Department of Materials Science and Metallurgical Engineering

University of Pretoria

Near-threshold fatigue crack growth behaviour of mild steel in steam during rotating bending

by

Ulyate Andries Curle

Submitted in partial fulfilment of the requirements for the degree

Master of Engineering
(Metallurgical Engineering)

in the

Faculty of Engineering, Build Environment and Information Technology

University of Pretoria

Pretoria

November 2006

Near-threshold fatigue crack growth behaviour of mild steel in steam during rotating bending

Candidate:	**Ulyate Andries Curle**
Supervisor:	**Prof GT van Rooyen**
Department:	**Materials Science and Metallurgical Engineering**
Degree:	**Master of Engineering (Metallurgical Engineering)**

Abstract

The influences of a superheated steam environment and temperature on the near-threshold crack growth behaviour of mild steel during rotating bending fatigue were investigated. A fatigue machine in which rotating bending is simulated was designed and built to allow continuous crack growth measurement. Experiments compared the threshold stress intensities (ΔK_{th}) for air at 24 °C, air at 160 °C and steam at 160 °C. Air at 160 °C yielded the lowest threshold stress intensity in both cases. Oxide thicknesses in the vicinity of the threshold were estimated from temper colours. The difference in threshold stress intensities can be explained by the concept of oxide-induced crack closure.

Keywords: rotating bending fatigue; near-threshold crack propagation; oxide-induced crack closure; environment; steam

TABLE OF CONTENTS

LIST OF FIGURES AND TABLES

1. INTRODUCTION

Turbine shafts often contain material defects which are important when a high degree of reliability is required, for instance when the expected life of the component may exceed 20 years. It is therefore important to predict the behaviour of such defects under service conditions. Transverse cracks can, for example, originate in turbine shafts by fretting of the disk collar and the shaft at keyways (Lindley, 1997). Such cracks could then propagate by fatigue due to rotating bending stresses imposed by the shaft's own weight. In addition, steam turbine shafts operate at temperatures above room temperature and in a steam environment, which can also influence the crack growth behaviour of small defects in the shaft.

2. A BRIEF HISTORY OF FATIGUE RESEARCH

Although the phenomenon of metal fatigue has been known for a very long time, it was not until the mid 1800s that serious scientific investigations were undertaken. Avoiding material damage and fatalities was and still is one of the main reasons to combat fatigue. Economic considerations are also important for companies that operate structures that are subjected to fatigue: when failures occur, they usually affect the downstream systems. Table 2.1 represents selected contributions to and events during the history of fatigue.

Table 2.1. Selected contributions to and events during the history of fatigue (after Schütz, 1996)

Date	Contributor	Contribution
1837	Albert	The first known fatigue results published
1842		Locomotive axle failed in Versailles, killing 60
1854	Braithwaite	The term "fatigue" mentioned the first time
1860	Wöhler	Results of fatigue tests with railway axles published
1880	Bauschinger	Bauschinger effect described
1903	Ewing & Humfrey	Slip bands on the surface of rotating bending specimens observed
1910	Basquin	The relation $\sigma_a = C \cdot R^n$ proposed
1917	Haigh	Corrosion fatigue experiments
1918	Douglas	Full-scale fatigue tests on aircraft components
1920	Griffith	Basis for fracture mechanics developed
1924	Gough	Book on fatigue, influence of surface roughness
1924	Palmgren	Damage-accumulation hypothesis
1930	Numerous contributors	Measuring of service stresses
1939	Rage & de Forrest	Electrical resistance strain gauge invented
1939	Weibull	Statistical scatter experiments
1941	Walz	Shot-peening suggested to improve fatigue life
1945	Gassner	High strength materials have unfavourable fatigue properties

	Miner	Damage accumulation hypothesis checked with fatigue tests
1954	Manson & Coffin	Plastic strain damage for low-cycle fatigue
		Third "Comet" aircraft crashes since May 1952
1958	Irwin	Stress intensity factor, $K = S\sqrt{\pi \cdot a}$. Linear elastic fracture mechanics (LEFM) born
		Two steam turbine rotors burst
~1960		Crash of an F-111 after only 100 flight hours
1962	Paris	Fatigue crack propagation described with $$\frac{da}{dN} = C \cdot \Delta K^n$$
1968	Elber	Crack closure concept
1974	USAF	Introduction of "Damage Tolerance Requirements"
1988		Near-fatal accident of an Aloha Airlines Boeing 737

3.   THEORETICAL BACKGROUND

3.1.   DEFINITIONS

Fatigue crack propagation is governed by the static stress, the dynamic stress applied and the crack length. In linear elastic fracture mechanics (LEFM) the stress distribution ahead of a crack is defined by the stress intensity parameter (K) (equation 1):

$$K = Y\sigma\sqrt{\pi a} \qquad \left[MPa\sqrt{m}\right] \qquad (1)$$

where Y is a geometric factor, σ is the monotonic applied stress and a is the crack length. K_{IC} is the critical stress intensity or the fracture toughness property of the material and defines the plain strain stress intensity at which a crack will propagate in a fast, unstable manner.

In fatigue, the applied stress is a time-dependent function. For the condition of constant amplitude loading, the parameters that describe the applied stress can be defined as shown in figure 3.1.
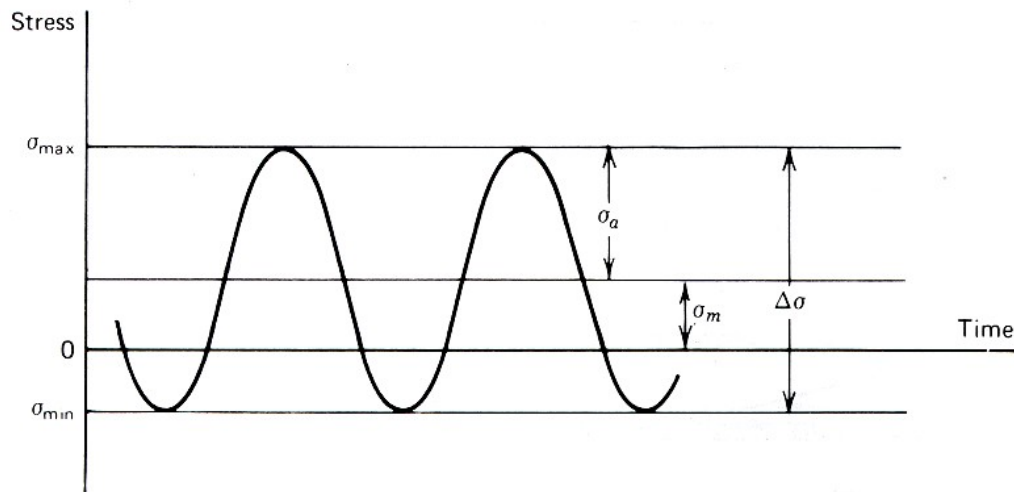
Figure 3.1. Description of a time-dependent stress function during constant amplitude cycling (Hertzberg, 1995)

Three parameters are defined in the graph above:

$$\Delta\sigma = \sigma_{max} - \sigma_{min} \qquad = \text{Stress range} \qquad (2)$$

$$\sigma_a = \frac{\sigma_{max} - \sigma_{min}}{2} \qquad = \text{Stress amplitude} \qquad (3)$$

$$\sigma_m = \frac{\sigma_{max} + \sigma_{min}}{2} \qquad = \text{Mean stress} \qquad (4)$$

$$R = \frac{\sigma_{min}}{\sigma_{max}}. \qquad = \text{Stress ratio} \qquad (5)$$

When the tensile and compressive components of the cyclic stress have the same magnitude R is equal to -1. This is the case for rotating bending fatigue where every portion of the surface of the shaft is subjected to the same stress cycle during one revolution. Turbine rotors and other rotating shafts are subjected mainly to this type of stress as a result of bending under the shaft's own weight. The shaft will also be subjected to a cyclic shear stress during every revolution. In addition, the turbine shaft also transmits torque and is therefore also subjected to a torsional stress of approximately constant value.

The cyclic stress intensity range (ΔK) for a constant cyclic stress amplitude can be defined as the difference between the maximum and the minimum stress intensities during fatigue when the crack length is a. Therefore:

$$\Delta K = K_{max} - K_{min} = Y \Delta \sigma \sqrt{\pi a} \qquad (6)$$

where K_{max} is the maximum stress intensity and K_{min} the minimum stress intensity during the loading cycle. The effective stress intensity range ΔK_{eff} can be defined as the stress intensity range that is the driving force for crack propagation:

$$\Delta K_{eff} = K_{max} - K_{op} \qquad (7)$$

where K_{op} represents the stress intensity at which the crack faces first separate as the stress is increased during the load cycle.

In the calculation of ΔK it is customary and convenient to assume that only the tension part of the cycle contributes to the crack propagation during the fatigue process. If the loading cycle has a compressive component, the crack faces will be pressed together; as far as crack propagation is concerned, this portion of the stress cycle is frequently disregarded by assuming $K_{min} = 0$ and therefore $\Delta K = K_{max}$. However, the influence of the compressive portion of the load cycle cannot be disregarded altogether as is seen from the literature survey.

The fatigue crack growth rate per cycle ($\frac{da}{dN}$), in mm/cycle, resulting from a cyclic stress intensity range (ΔK) is determined by measuring the average crack growth for a fixed number of stress cycles. Figure 3.2 is a representation of typical crack growth data where the crack length is recorded as a function of the number of fatigue cycles.
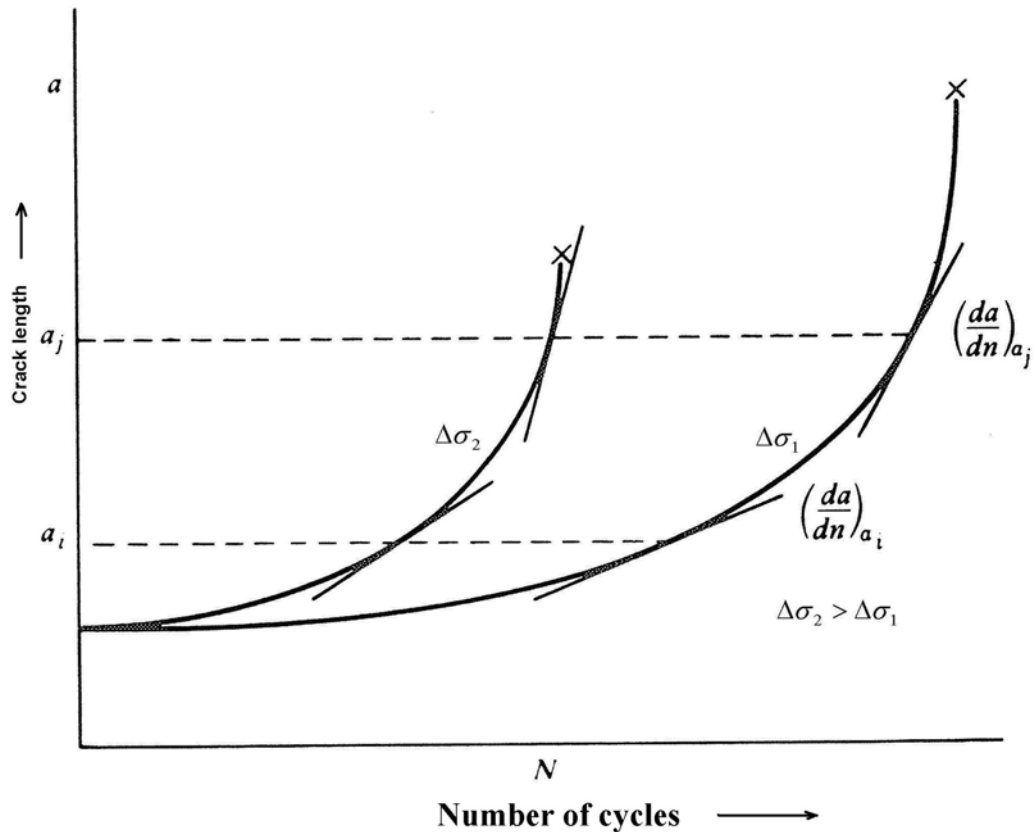
Figure 3.2. Crack growth data at two different cyclically applied stresses (Hertzberg, 1995)

The fatigue crack growth rate (FCGR) is usually determined by using the tangent to the crack growth curve or by an incremental polynomial method described in ASTM 647-99. It is seen from the figure above that for the same crack length, the FCGR is higher when the cyclic stress range is larger.

Crack growth rate data can then be graphically presented as a function of the cyclic stress intensity range (ΔK) on a log-log scale plot. The general features of such a curve are shown in figure 3.3. The curve has a sigmoidal shape with two asymptotes terminating the curve at very high and at very low stress intensity ranges.

At high ΔK levels, K_{max} approaches the fracture toughness of the material (K_{IC}), where the specimen fractures at an uncontrollable rate. In the mid-ΔK range it is accepted that the linear behaviour can be described by the Paris relation $\dfrac{da}{dN} = A\Delta K^m$, where A and m are material constants. The asymptote at low ΔK levels defines the threshold stress intensity (ΔK_{th}). ΔK_{th} defines the point where crack growth essentially stops or the FCGR decreases to low values, of the order of 10^{-7} mm/cycle or less. This value is then defined as an operational threshold value according to ASTM 647-99. Even at very low rates, crack propagation is important; for instance in the case of high-cycle fatigue, where a turbine shaft during a lifetime of say 20 years may be subjected to 3×10^{10} fatigue cycles.
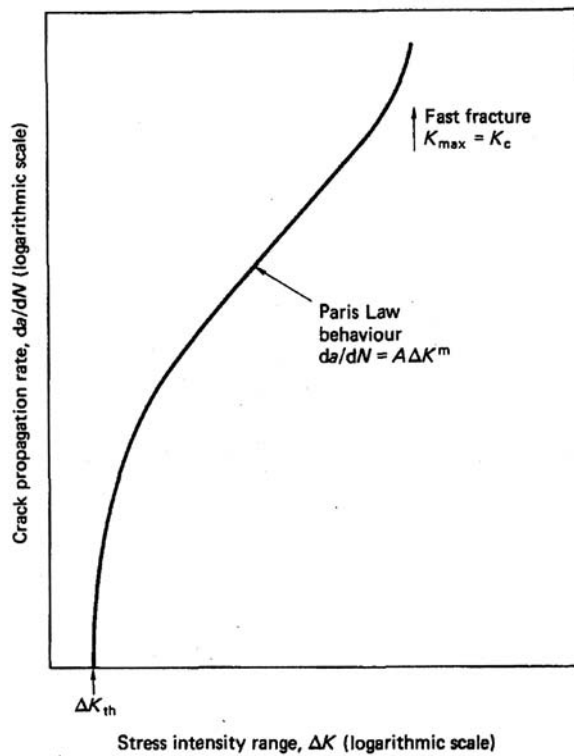
Figure 3.3. Crack growth rate as a function of the stress intensity range (Taylor, 1988)

3.2. RELEVANT TERMS

The **loading mode** describes the geometric orientation of the crack faces relative to the orientation of the applied stress. Figure 3.4 shows the three basic modes of loading.
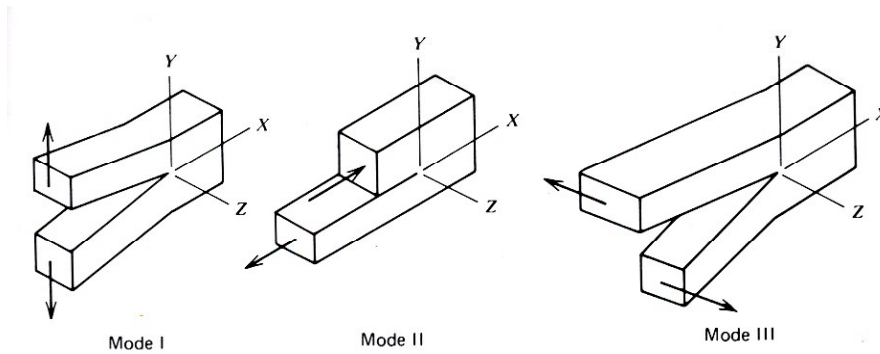
Figure 3.4. Different loading modes (Hertzberg, 1995)

In the case of rotating bending where the cyclic shear stress is zero (pure bending moment), crack propagation occurs in the crack opening mode (Mode I) and crack propagation can be expected when the bending stress at a particular point reaches a maximum tensile value. Crack propagation will always occur at right angles to the direction of the principal tensile stress, and consequently the crack orientation at the surface can be expected to be transverse to the longitudinal direction of the shaft when the shear stress and torsional moment are zero. This will, however, be affected by the presence of a torsional moment and the cyclic shear stress to which the shaft may be subjected. At the maximum crack opening orientation, the stress condition the surface can be illustrated with a Mohr circle (figure 3.5).
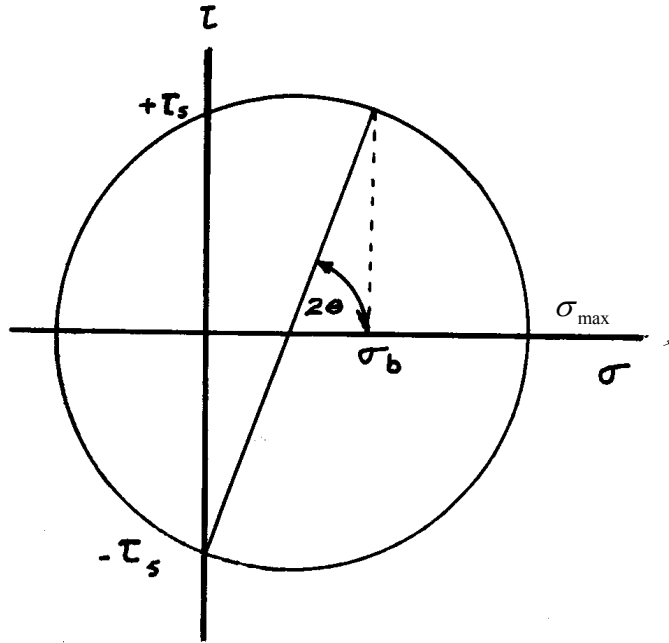
Figure 3.5. **Mohr circle representing the stress in the maximum crack opening orientation**

(σ_b = **bending stress and** τ_s = **torsional shear stress**)

In the presence of shear loading, crack propagation can then be expected along a helical path oriented at an angle θ with respect to the transverse direction. As a fatigue crack propagates when the cyclic shear stresses due to shear forces are no longer negligible in comparison with the bending stress, the increasing magnitude of the cyclic shear stress will also affect the orientation of the crack and cause the angle θ to increase further. The situation is further complicated by possible crack propagation in the crack tearing mode (Mode III) when the shaft with a crack has turned through a further 90° from the fully crack opening position. This can in some instances result in a crack surface with an increasingly ratcheted surface as the crack progresses towards the centre of the shaft.

Crack closure is a term used to describe the condition when there is an obstruction in the crack wake that prevents the crack faces from separating immediately when the applied stress is increased. Crack closure therefore reduces the effective cyclic stress intensity (ΔK_{eff}). Crack closure therefore reduces the portion of the cyclic stress amplitude when the crack faces are apart and the crack is consequently able to

9

propagate. There are three main crack closure mechanisms that influences fatigue threshold behaviour:

Plasticity-induced crack closure occurs when the compressive residual stress of the plastic zone that forms in front of the crack tip during unloading produces crack closure, preventing the crack from extending. This is particularly the case when an overload fatigue cycle is followed by regular fatigue crack testing at a lower cyclic stress.

Roughness- or asperity-induced crack closure occurs when the fracture facets on opposite crack faces do not fit well when the crack faces close as the applied stress is decreased. Evidence of this is when rubbing of the crack faces result in a shiny fracture surface. This type of behaviour can be expected when there are complex movements of the crack faces such as may be expected during rotating bending where there are also high cyclic shear stresses due to shear forces and torsional moments.

Oxide- or debris-induced crack closure is found when some extraneous material, usually corrosion or oxidation products, is present in the crack wake preventing the crack from fully closing again after incremental crack propagation.

4. LITERATURE SURVEY

The threshold cyclic stress intensity (ΔK_{th}) at the operating temperature is of critical importance in assessing the reliability with which a turbine shaft can be operated. If the cyclic stress intensity range is less than the threshold value, further crack propagation is not expected. To obtain reliable values, testing would have to be done with a loading cycle that simulates the cycle to which the shaft is subjected in practice. At the same time it would require the experiments to be done in a steam environment at operating temperatures and pressures. Whereas it is feasible to do experiments in a steam atmosphere at various temperatures at atmospheric pressure, conducting experiments at the pressures encountered in a steam environment is much more difficult. As a first approximation to simulate real operating conditions, experiments can be conducted at the operating temperature but at atmospheric pressure, provided the steam is superheated.

4.1. ENVIRONMENT

In a study by Tu & Seth (1978) on the effect of a steam environment at 260 °C, it was found that ΔK_{th} was higher than in air at the same temperature (figure 4.1). The increase is attributed to an embrittlement process that causes crack branching, which in turn reduces the crack tip driving force. This embrittlement process is mentioned as opposed to blunting, which is a dissolution process at the crack tip. Branched cracks were found in the fast crack growth region as well as in the threshold region, although to a lesser extent in the latter region. In the case of testing in the steam environment a black corrosion product formed on the crack faces. It was argued that the dense corrosion product may reduce the diffusion of steam to the crack front, thereby reducing crack branching in the near-threshold region. The influence of the steam environment can be due to both the nature of the oxide that forms at the crack tip as well as modification of the mechanism of crack propagation when crack branching occurs. The view was expressed that crack branching probably has a much larger effect than the crack closure effects due to the presence of oxides.
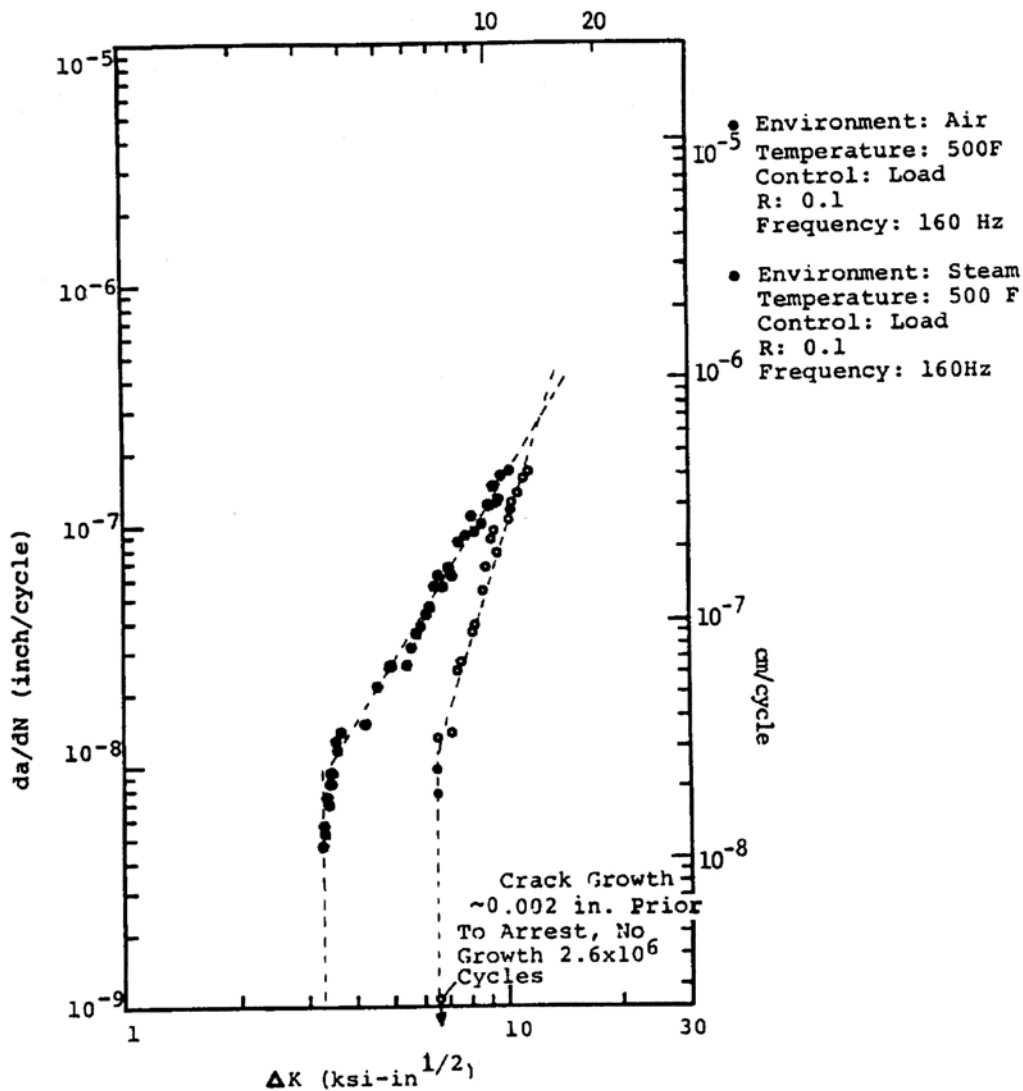
Figure 4.1. The influence of steam and air at 260 °C on ΔK_{th} (Tu and Seth, 1978)

In another study (Smith, 1987) on a 2NiCrMoV rotor steel in moist air and in dry air environments respectively at room temperature with $R = 0.14$, it was found that ΔK_{th} was higher for the moist air environment than for the dry air environment. This in turn was attributed to the formation of oxide debris near the threshold region causing oxide-induced crack closure (figure 4.2). In the same study the fatigue thresholds were first determined separately for both dry and moist air environments. In a subsequent test the effect of a change from dry to moist to dry air was studied using a constant ΔK value, with $\Delta K_{th}^{\,dry\ air} < \Delta K < \Delta K_{th}^{\,moist\ air}$. It was found that the crack growth rate in dry air first followed the dry air curve, but when the moist air was admitted crack growth was arrested, even after dry air was subsequently readmitted. From this it appears that once a fatigue threshold has been established in

12

a specific environment, further crack propagation will not take place when the environment is subsequently changed to an environment with a lower fatigue threshold. This is probably due to the fact that the crack closure effect due to the moist environment is maintained even after the environment is changed to dry air.
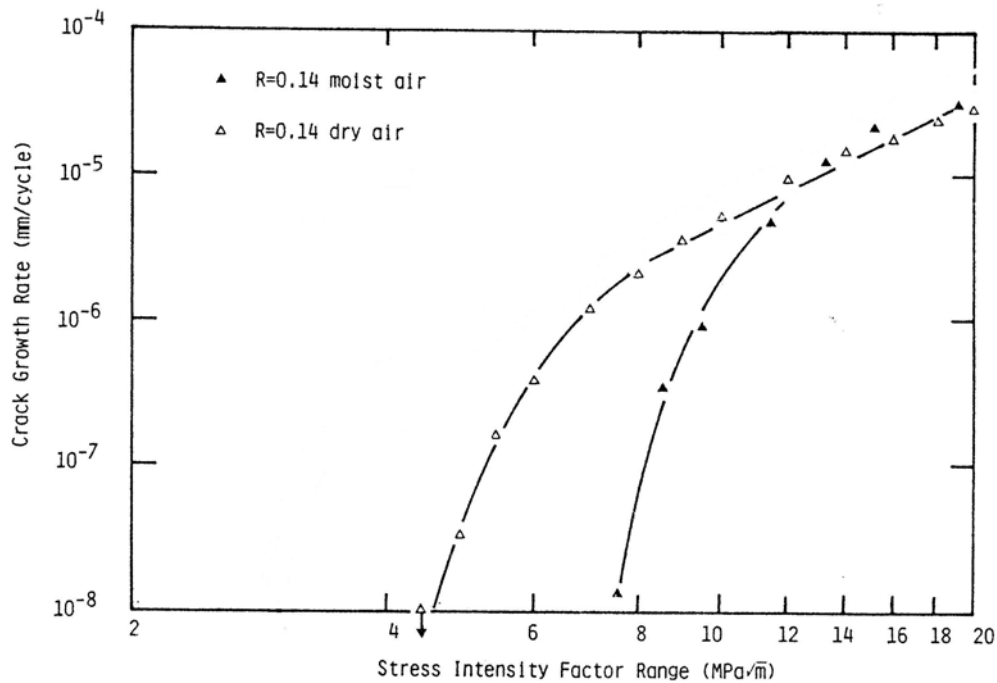
Figure 4.2. The influence of moist air and dry air for 2NiCrMoV steel on ΔK_{th} **(Smith, 1987)**

The environmental effects in different dry and moist environments were also evaluated for bainitic 2.25Cr-1Mo pressure vessel steel with $R = 0.05$ at room temperature (Suresh and Ritchie, 1983). Air was used as a reference for subsequent experiments in distilled water, wet hydrogen and dry hydrogen. It was found that for all the wet environments, including hydrogen, ΔK_{th} was higher than in a dry (hydrogen) environment (figure 4.3). The corrosion products on the fracture surface were identified as Fe_2O_3. This is another example of oxide debris wedging the crack open and thus contributing to oxide-induced crack closure. Hydrogen-assisted cracking can be ruled out, since even in wet hydrogen the threshold was higher than that in dry hydrogen.
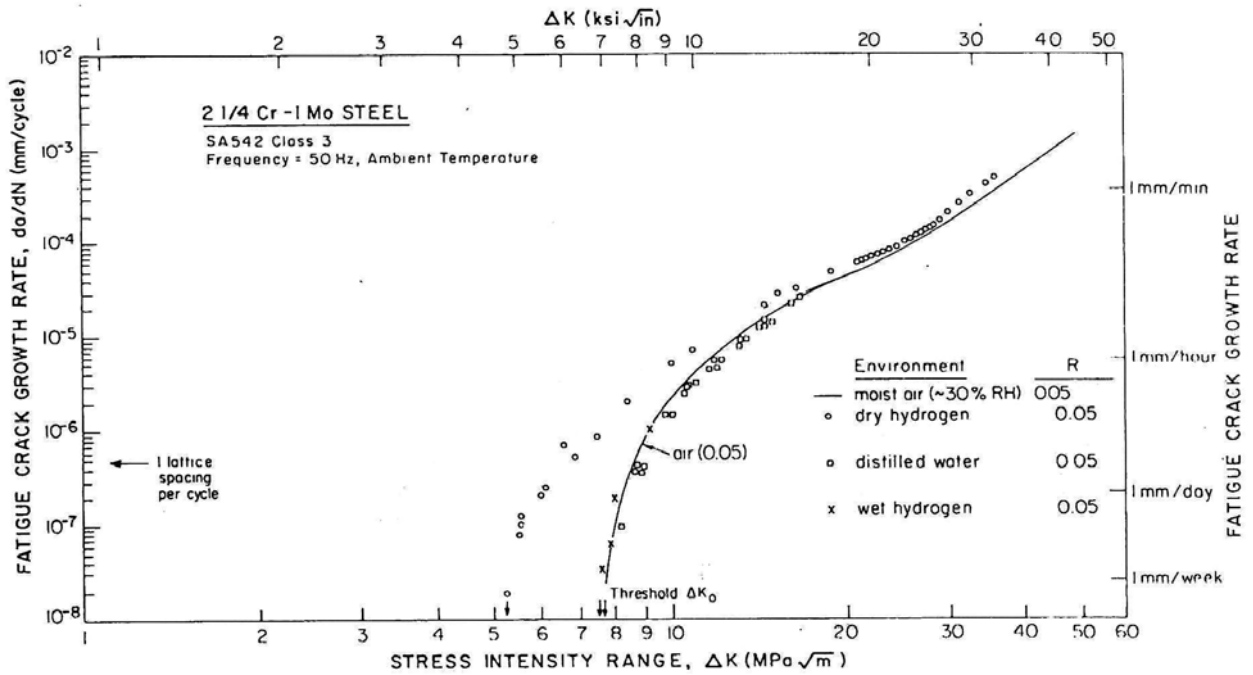
Figure 4.3. The influence of wet and dry environments on ΔK_{th} (Suresh and Ritchie, 1983)

4.2. TEMPERATURE

Experiments in air at different temperatures have shown that ΔK_{th} is dependent on temperature. At elevated temperatures there is a temperature range where the threshold stress intensity reaches a minimum value. This behaviour has been found in both A508-3 steel (Kobayashi) and in a CrMoV steel (Liaw, 1985). Figures 4.4 and 4.5 show the results of Liaw and Kobayashi respectively. These experiments were conducted over the temperature range of 24˚C to 427˚C. Liaw used a frequency of 60 Hz with $R = 0.1$ and Kobayashi used 25 Hz with $R = 0.05$. Figure 4.6 summarises Liaw's findings and explains the mechanisms underlying the temperature effect.
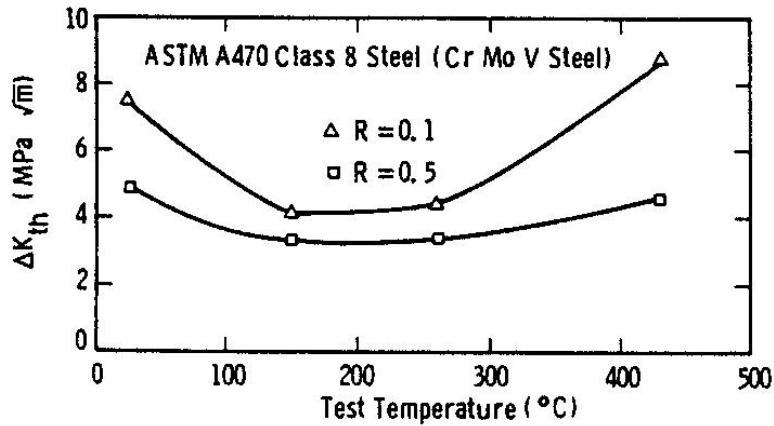
Figure 4.4. The effect of temperature on ΔK_{th} (Liaw, 1985)
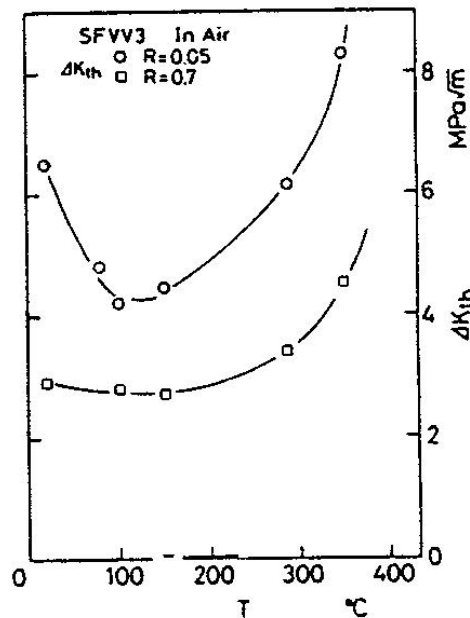
Figure 4.5. The effect of temperature on ΔK_{th} (Kobayashi et al, 1991)

The following reason was advanced for this behaviour. At room temperature ΔK_{th} is high due to a rougher fracture surface which interferes during the closing part of the cycle to cause roughness-induced crack closure. At intermediate temperatures, i.e. ~150°C, ΔK_{th} reaches a minimum value due to the formation of a stable thin oxide layer on the crack faces and a reduction in surface roughness. In the high-temperature region the oxide layer thickness increases again due to thermal oxidation that produces crack closure and then results in higher ΔK_{th} values. This is schematically illustrated in figure 4.7.
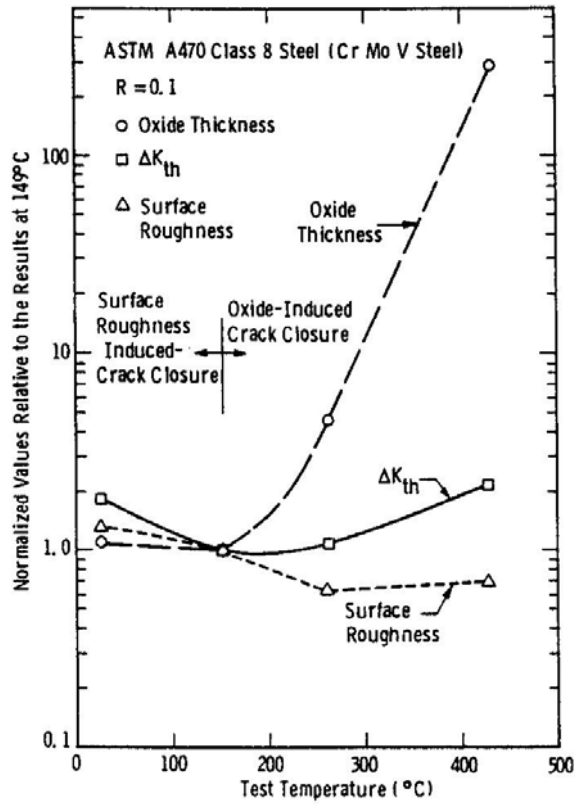
Figure 4.6. Summary of the effect of temperature on ΔK_{th} (Liaw, 1985)
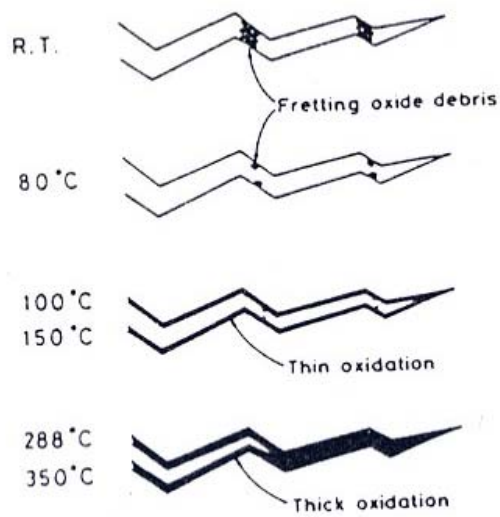
Figure 4.7. Diagrammatical illustration of the temperature effect on ΔK_{th} (Kobayashi, 1991)

16

4.3. STRESS RATIO (R)

The general trend observed in stress ratio studies is that as R is increased, ΔK_{th} decreases. As stated earlier, R is a measure of the mean applied stress. The influence of R can also be explained by the concepts of crack closure. At the low end of R oxide- and roughness-induced crack closure dominate, since the crack faces come into close contact. However, at the high end of R the effect of crack closure is reduced due to the high mean loads causing the crack faces to stay apart and therefore reducing the crack closure effect.

An example of the influence of R on ΔK_{th} is seen in a study (Suresh and Ritchie, 1983) where $0.05 \leq R \leq 0.75$ was used in an air environment at room temperature for an SA542-3 steel (figure 4.8). The same trend can be seen in figures 4.4 and 4.5.
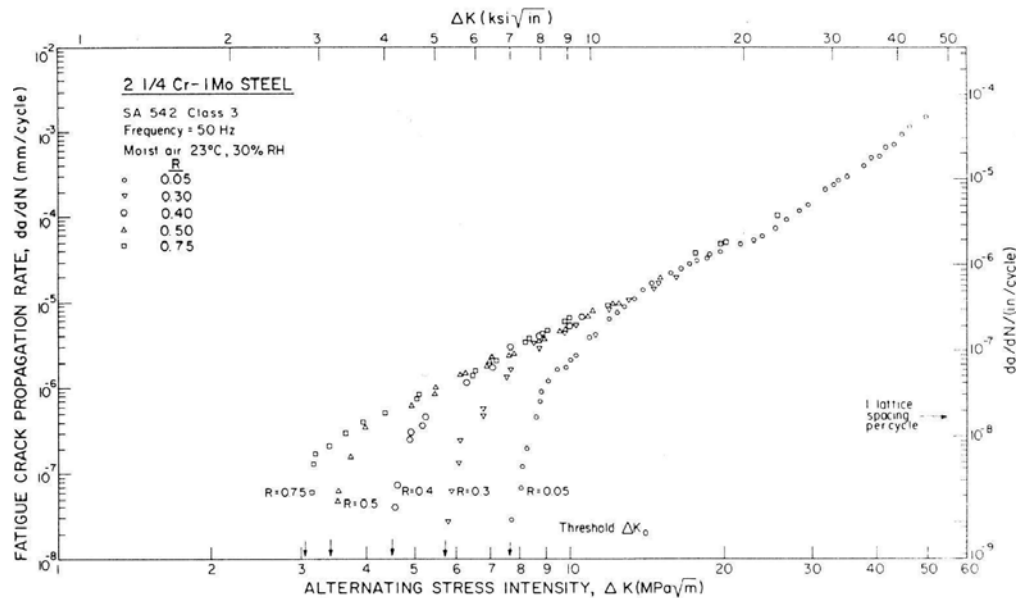
Figure 4.8. The influence of R on ΔK_{th} (Suresh and Ritchie, 1983)

Usually crack propagation tests are conducted with $R \geq 0$. In the case of rotating bending $R = -1$, and it is important also to know what happens at negative values of R. The influence of negative R values is shown in figure 4.9 (Lindley, 1981). The solid lines for $R < 0$ represent the possible condition where K_{min} is taken as negative for the compressive part of the cycle. This will cause ΔK to become larger and consequently result in an increase of ΔK_{th} as R becomes more negative. On the

other hand, the dashed lines represent the usual dependence of ΔK_{th} on R as $\Delta K = K_{max}$ with $K_{min} = 0$ for the compressive part of the cycle.
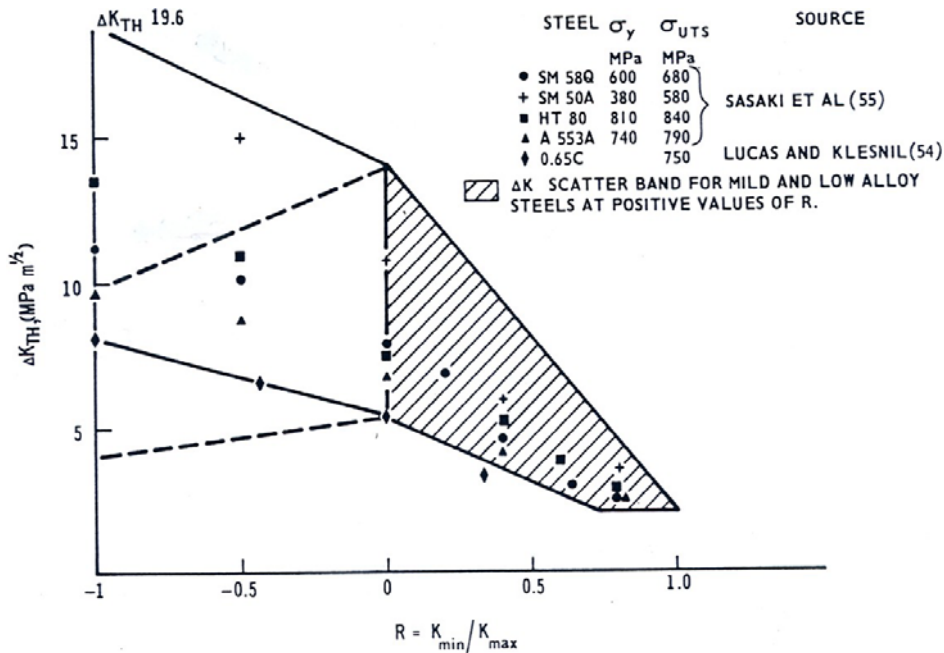
Figure 4.9. The effect of stress ratio on ΔK_{th}, with negative values of R (Lindley, 1981)

4.4. COMPRESSIVE LOADS

During rotating bending fatigue, one half of the stress cycle is compressive and the other half tensile. According to ASTM 647-99, it is recommended that only the tensile part of the load cycle be taken into consideration in the calculation of ΔK neglecting the compressive half of the cycle. A number of studies investigating the influence of the compressive portion of the loading cycle suggest that this assumption could lead to non-conservative predictions of ΔK_{th} obtained from testing where $K_{min} = 0$. In these studies, it was found that the magnitude of the compressive stress cycle as well as the number of cycles between compressive stress cycles has an influence on ΔK_{th}.

In a study by Zaiken et al (1985) using I/M 7150 aluminium alloy in the underaged-, peak and overaged condition thresholds were first determined with

18

$R = 0.1$. Thereafter a single compressive load was applied and the test was resumed at $\Delta K = \Delta K_{th}$ with $R = 0.1$. It was observed that further crack growth occurred subsequent to the single compressive load cycle (figure 4.10). Further crack growth stopped after the crack had progressed by 60 to 170 μm, depending on the ageing condition. It was found that compressive loads down to $3 \times K_{max}$ did not result in further crack growth. Only when the compressive cycle was equal to $5 \times K_{max}$ was there an effect. The same observations were also made for SAE1010 steel. One sample was used to determine a reference crack growth rate curve with $R = 0$. The second sample was then cycled at a low ΔK value, also with $R = 0$, and gave an FCGR similar to the reference curve. Three compressive load cycles were then applied with a magnitude equal to $3 \times K_{max}$, after which the test was resumed. The FCGR increased relative to that of the reference curve, and only after 6.67×10^5 further cycles did the FCGR decrease to the original value of the reference curve.

A saturation compressive cycling effect was reported for Cu and two Al alloys in a study (Kemper et al, 1989) where ΔK_{th} was determined with R ranging from -10 to $+0.8$ defining $\Delta K = K_{max}$ for $R < 0$ and $\Delta K = K_{max} - K_{min}$ for $R > 0$. Decreasing the value of R towards more compressive loading did not decrease ΔK_{th} beyond a certain limit, as shown for Cu in figure 4.11. In all the samples, this saturation limit was found to occur at $R \approx -2$. The reduction in the threshold stress intensity values as R becomes more negative was attributed to the reduction of roughness-induced crack closure due to the plastic flattening of asperities during the compression portion of the cycle.
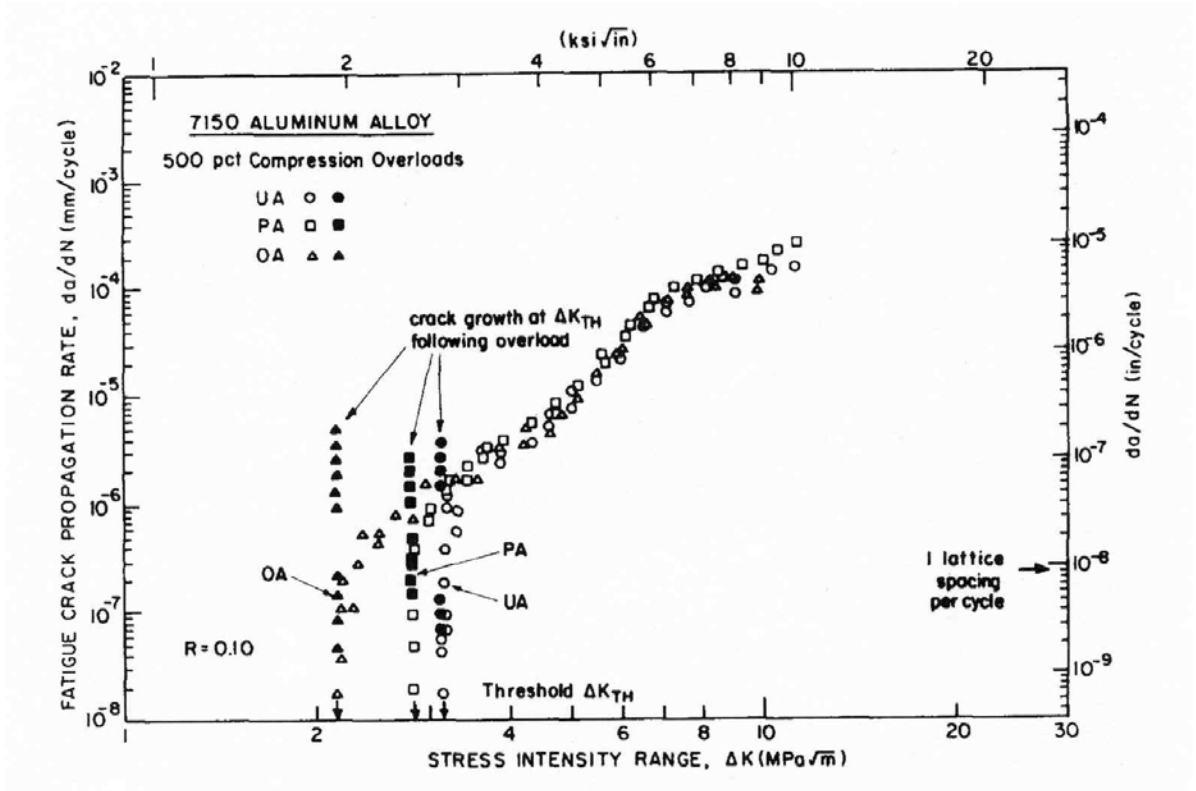
Figure 4.10. Increase in the crack growth rate (closed symbols) when cycled at $\Delta K = \Delta K_{th}$ with $R = 0.1$ after a single $5 \times K_{max}$ compressive load for underaged (UA), peak aged (PA) and overaged (OA) 7150 Al alloy samples (Zaiken et al, 1985)
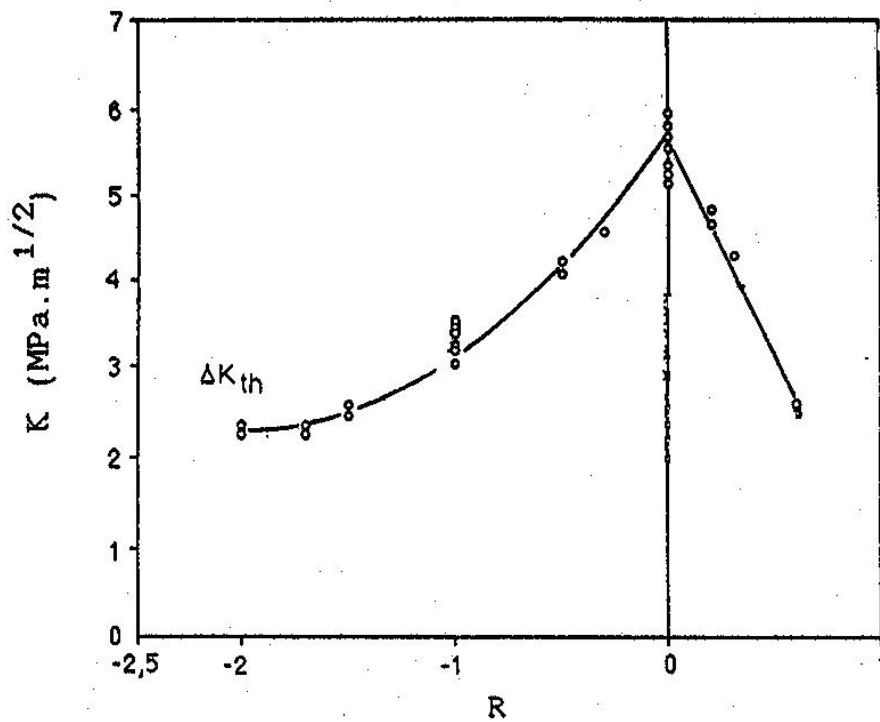
Figure 4.11. Influence of stress ratio on the fatigue threshold of recrystallised Cu (Kemper et al, 1989)

For Waspaloy, an aluminium powder metallurgy alloy IN-9052 and bearing steel M50NiL (Carlson et al, 1994) it was found that the crack growth rate increased sharply when the stress ratio was changed to $R = -2$ after cycling at $R = 0.1$. The above study did not consider compressive stress cycle effects on the threshold stress intensity value, but focused on the influence of compressive stress cycle effects on FCGR (loading sequence shown in figure 4.12). There is a clear indication that compressive cycling increases the crack growth rate for a given ΔK when ΔK_{min} is defined as $\Delta K_{min} \geq 0$. This behaviour was attributed to the inelastic crushing of asperities, resulting in a decrease of roughness-induced crack closure.
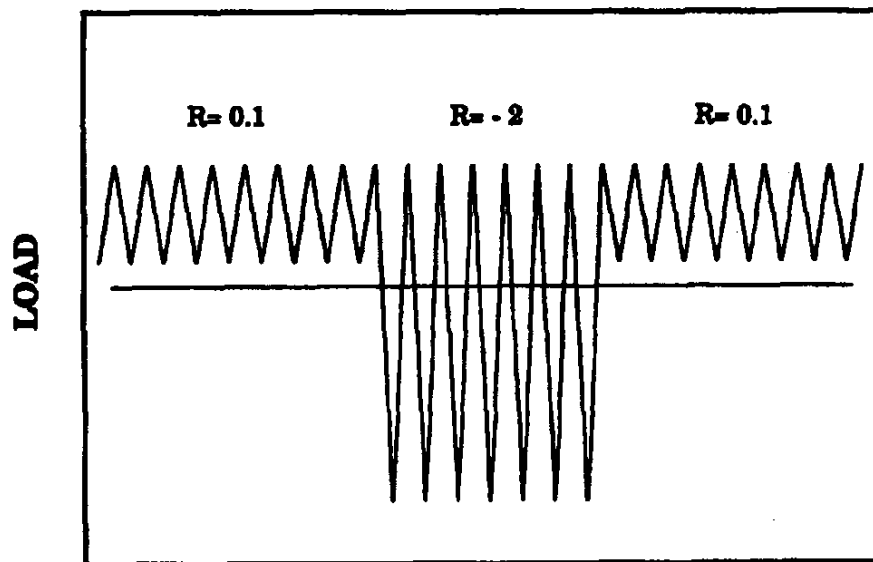
Figure 4.12. Loading sequence to assess crack growth behaviour of alternate compressive load cycling (Carlson et al, 1994)

Topper et al (1985) investigated the effect of intermittent compressive stress cycles on aluminium and steel. It was found that as the number of cycles between successive compressive stress cycles during a test with $R = 0$ increased, the threshold value increased (see Figure 4.13). When the number of compressive stress cycles during the test was zero, the threshold ΔK_{th} was at a maximum value, but when compressive stress cycles were applied during each cycle the threshold decreased to a minimum value. In CSA G40.21 steel, ΔK_{th} decreased from $7.2 MPa\sqrt{m}$ for no compressive

stress cycles to $3.5 MPa\sqrt{m}$ when each cycle contained a compressive stress cycle component as shown in figure 4.13.
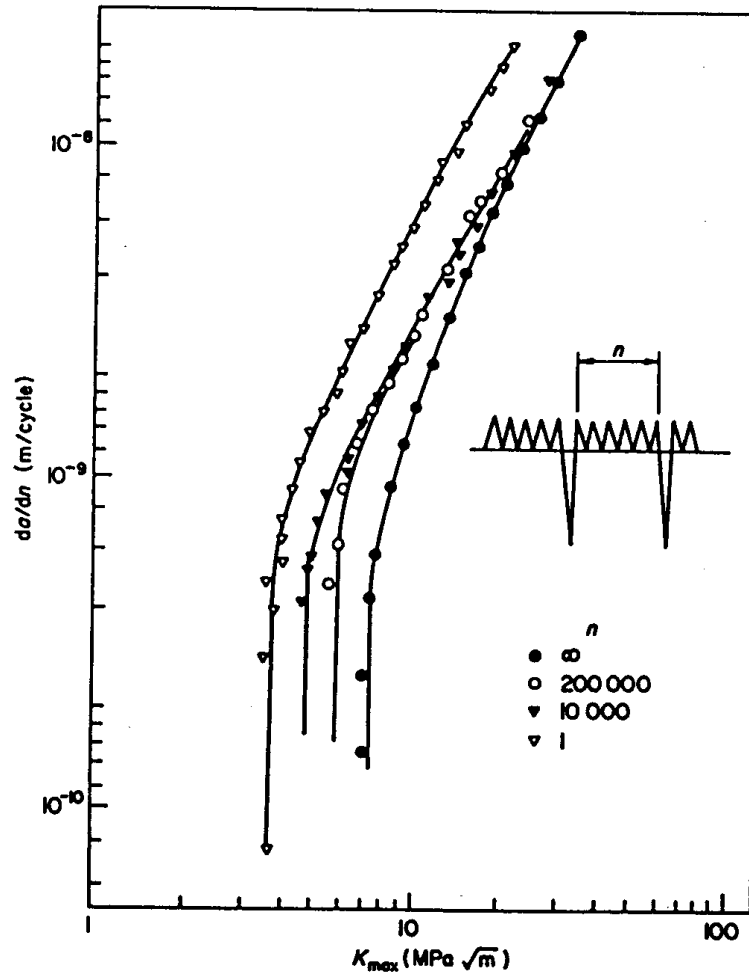
Figure 4.13. Decreasing the interval between compressive stress cycles decreases ΔK_{th} in CSA G40.21 steel (Topper et al, 1985)

From this it is concluded that compressive stress cycles also influence ΔK_{th}, especially if crack closure is a dominant feature. If a material does not exhibit a large crack closure effect (for instance when it has a very small grain size), the ASTM recommendation would apply, since the compressive stress cycle – within limits – then does not influence the effective stress intensity to any large extent.

22

4.5. RESIDUAL STRESS

Because of the difficulties encountered in measuring residual stress fields (Lawson et al, 1999), the literature on the influence of residual stresses on ΔK_{th} is not very extensive. However, residual stress fields can be expected to influence the FCGR. The threshold value in particular is very sensitive to any change in ΔK_{eff}. The nature of the plastic zone formed during the fatigue loading sequence of a crack also results in a local residual stress system that would be modified by the longer-ranging original residual stresses. Upon unloading after a tensile overload, for example during fatigue, the stress state around the crack tip results in a larger zone with a very high compressive stress. When cycling is resumed at the previously lower stress intensity range, the crack growth is retarded, and the original crack growth per cycle is only reached after the crack has proceeded beyond the compressive stress field set up by the overloading. If the applied stress intensity is not large enough to cancel the compressive stress field, the crack could arrest completely. This effect is also observed when threshold values are artificially high because the load-shedding rate which causes plasticity-induced crack closure is high.

Residual stress fields have a marked influence on the profile (shape) of the fatigue crack front, illustrating the influence they can have on ΔK_{th} and to a lesser extent on ΔK. This behaviour was observed in a study by Geary et al (1987) investigating the influence of tempering temperature on a quenched and tempered low alloy boron steel. Figure 4.14 shows the measured residual stress distribution across the specimen, while figure 4.15 shows the actual crack front profile at the threshold. As an approximation, the residual stress field can be considered to be superimposed onto the applied stress field, changing the local value of R.
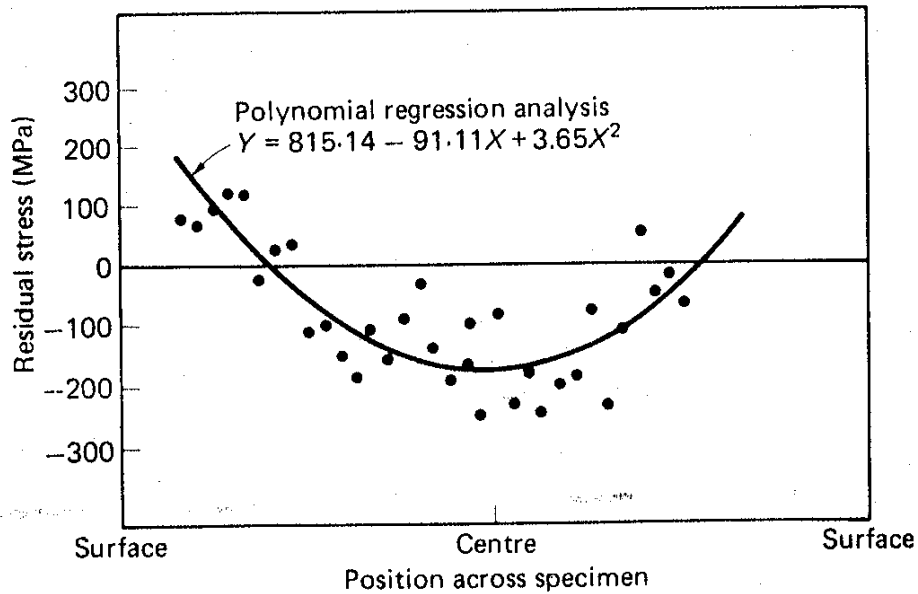
Figure 4.14. Measured residual stress distribution across a quenched and tempered specimen (Geary et al, 1987)
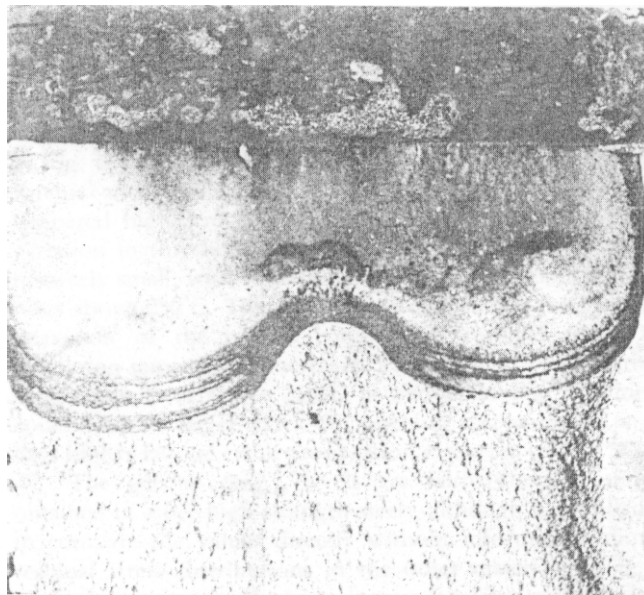
Figure 4.15. Actual crack front profile of a specimen austenitised at 900 °C, quenched in water and tempered at 20 °C (Geary et al, 1987)

4.6. TEST CYCLE FREQUENCY

It has been shown (Bignonnet et al, 1982) that there is a decrease in the threshold stress intensity with decreasing test frequency. In tests conducted in air at room

24

temperature, fretting oxidation was advanced as the mechanism to explain the increase of the FCGR at higher test frequencies. Although the near-threshold condition was not considered, an extrapolation of their results for testing at 65Hz and 7Hz would probably result in a higher threshold value for 65Hz compared with a threshold value for 7Hz (figure 4.16).
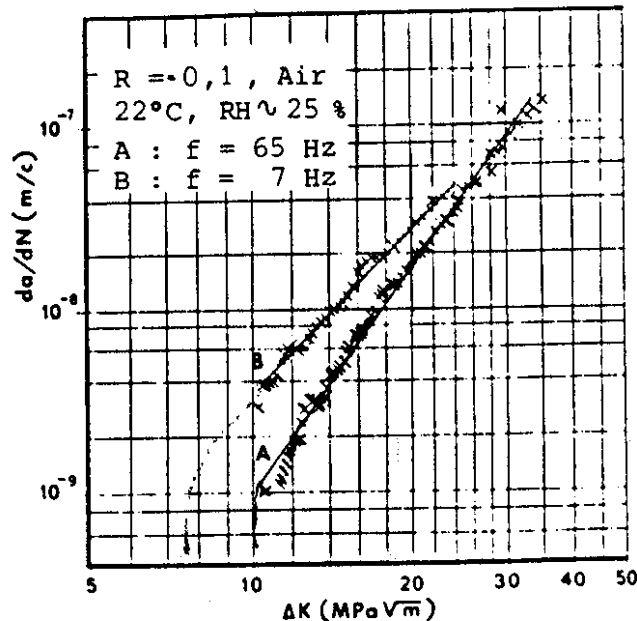
Figure 4.16. Effect of test frequency on the fatigue crack growth rate (Bignonnet et al, 1982)

4.7. GRAIN SIZE

Grain refinement has been used to increase the strength as well as the fatigue limit of materials. This effect is thought to be due to an increase in the number of obstacles that will retard crack initiation. However, this is not the case during near-threshold crack propagation, where ΔK_{th} increases with the grain size (Lawson et al, 1999).

Data in the literature (Lindley, 1981) indicates that lower-strength steels in general have a higher threshold value than high-strength steels (figure 4.17). The influence of grain size on ΔK_{th} can be explained partially by the fact that the strength of the steel increases as the grain size decreases. A decreased grain size can also produce a smoother fracture surface and therefore have less of a crack closure effect.
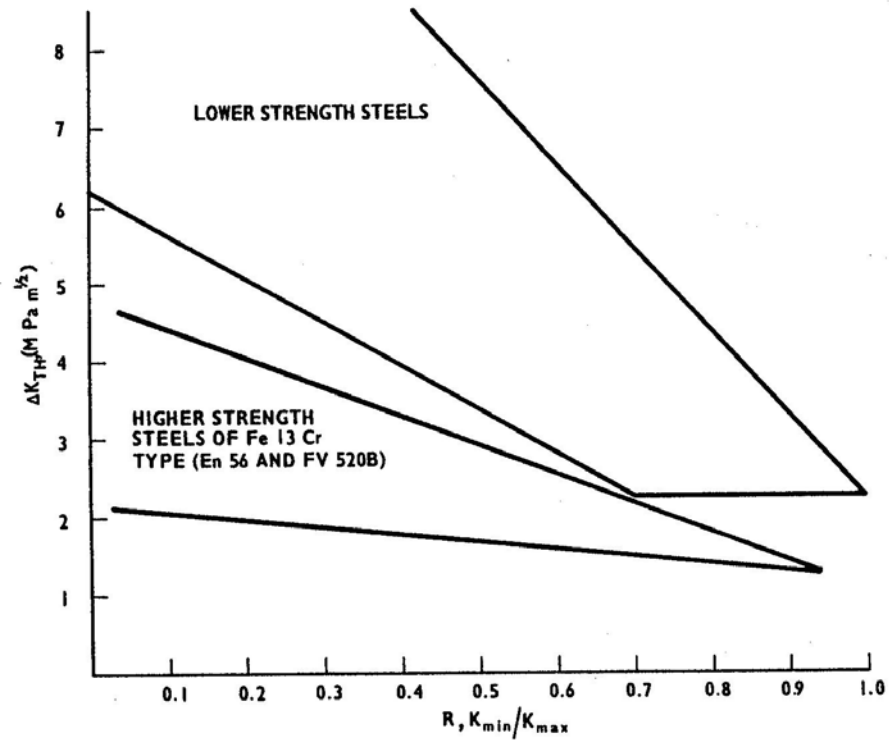
Figure 4.17. Collective threshold data for high- and low strength steels as a function of R (Lindley, 1981)

In a study by Masounave et al (1976) on a ferritic steel it was shown that the effect on ΔK_{th} is directly proportional to the square root of the grain size, as shown in figure 4.18.
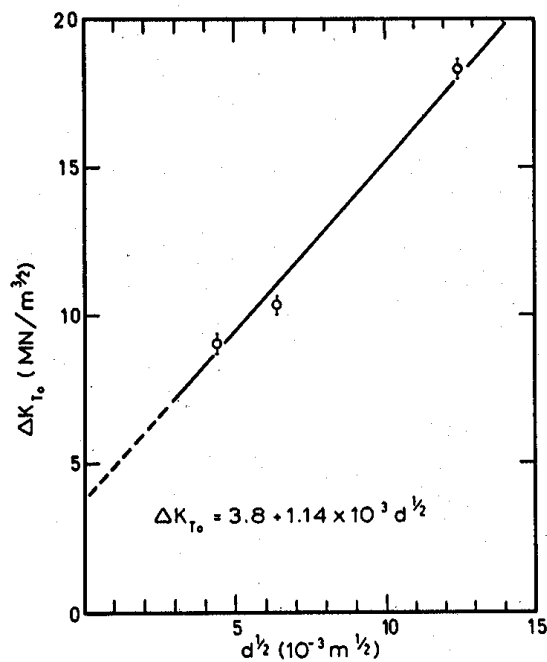
Figure 4.18. Effect of grain size on the threshold stress intensity (Masounave et al, 1976)

26

4.8. CONCLUSION

From the literature search it can be concluded that most of the ΔK_{th} effects can be related to crack closure mechanisms. If the environment is high-temperature steam, the mechanism seems to be branching of the crack front (Tu & Seth, 1978) as well as a buildup of corrosion products, both of which decrease the effective stress intensity. In steam a higher resistance to crack propagation is expected and consequently also a higher fatigue threshold value.

5. MACHINE DESIGN

5.1. ROTATING BENDING

Rotating bending is normally carried out with RR Moore-type rotating bending machines (Czyryca, 1985), in which the gauge length of the specimen is subjected to a pure bending moment. The cyclic stress in a rotating shaft can, for example, also be simulated by suspending a dead load from the free end of the rotating shaft. At the position where the specimen fails the material will – apart from a cyclic bending stress – also be subjected to a smaller cyclic shear stress. To establish the fatigue threshold stress intensity, the bending moment on pre-cracked specimens is reduced until a point is reached where the specimen never breaks. Although the setup is simple, it is expensive and time consuming due to the large number of samples required.

Uniaxial servo-hydraulic machines, in a way, simulate rotating bending when the stress ratio (R) is equal to -1. These types of tests do not fully mimic the shear interaction of the crack faces during rotating bending, where large cyclic shear stresses may also be present. One of the disadvantages of the above method is the presence of mechanical backlash in the setup as the load passes the zero load line from tension to compression. Another disadvantage is that misalignment can easily result from buckling of the sample during the compressive part of the cycle. Consequently, a need exists for a machine that can simulate the complex crack face movement encountered during rotating bending of an actual shaft and also allows continuous crack measurement.

For this purpose it was necessary to design and build a customised fatigue-testing machine. The design provides for a round specimen that is rigidly clamped at the one end whilst the other end is subjected to a circular motion by means of an eccentric drive. The aim of this design is to produce a loading sequence of tension and compression, at the tip of the crack, of equal magnitude; this means that $R = -1$. The fact that the specimen itself does not rotate enables the continuous monitoring of crack propagation during testing.

5.2. DESIGN OF FATIGUE TESTING MACHINE SIMULATING ROTATING BENDING

Figure 5.1 shows the custom-built fatigue-testing machine on the left with its steam generating system at top right.
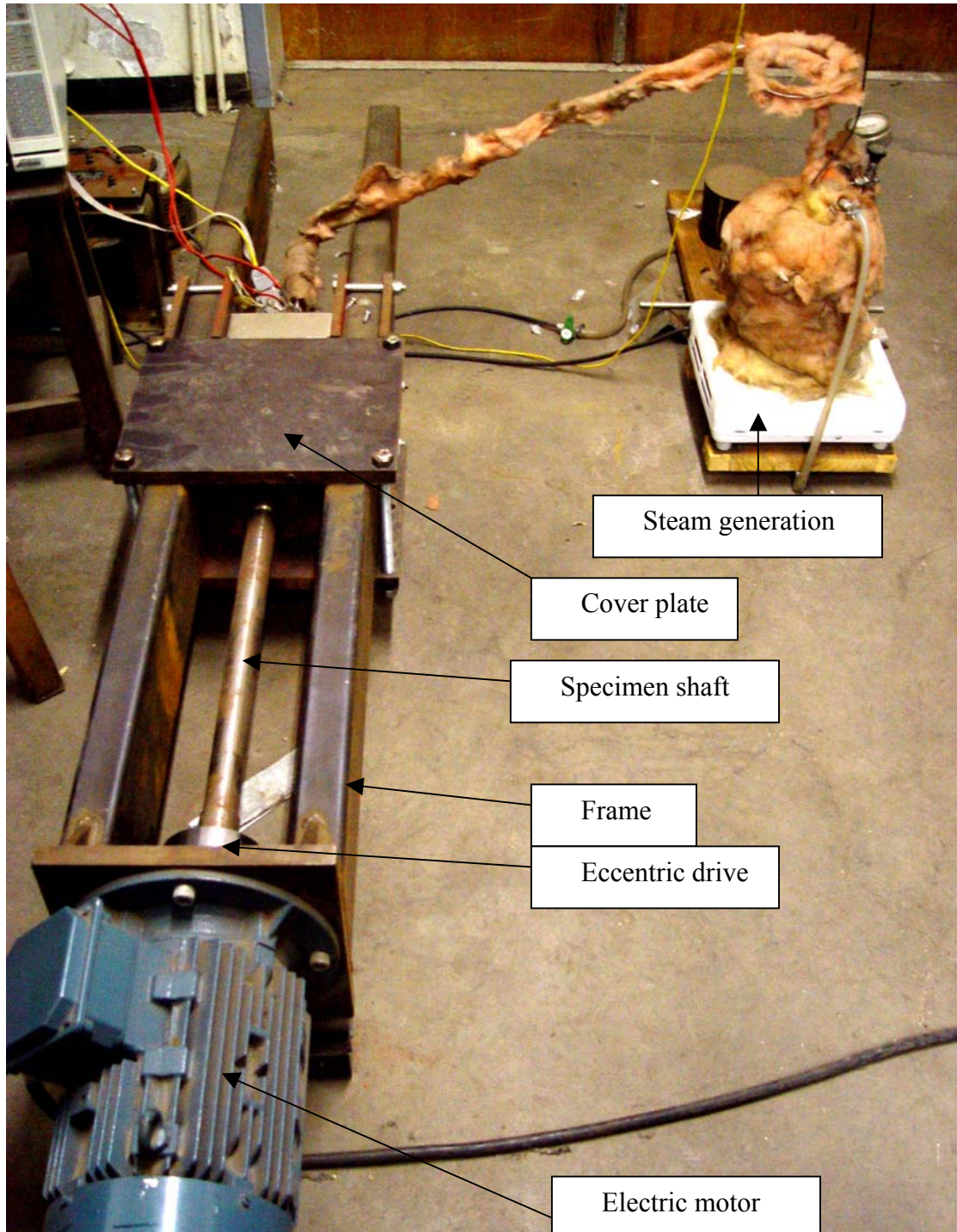
Figure 5.1. Setup of the fatigue-testing machine

Figure 5.2 is an isometric drawing of the machine setup.
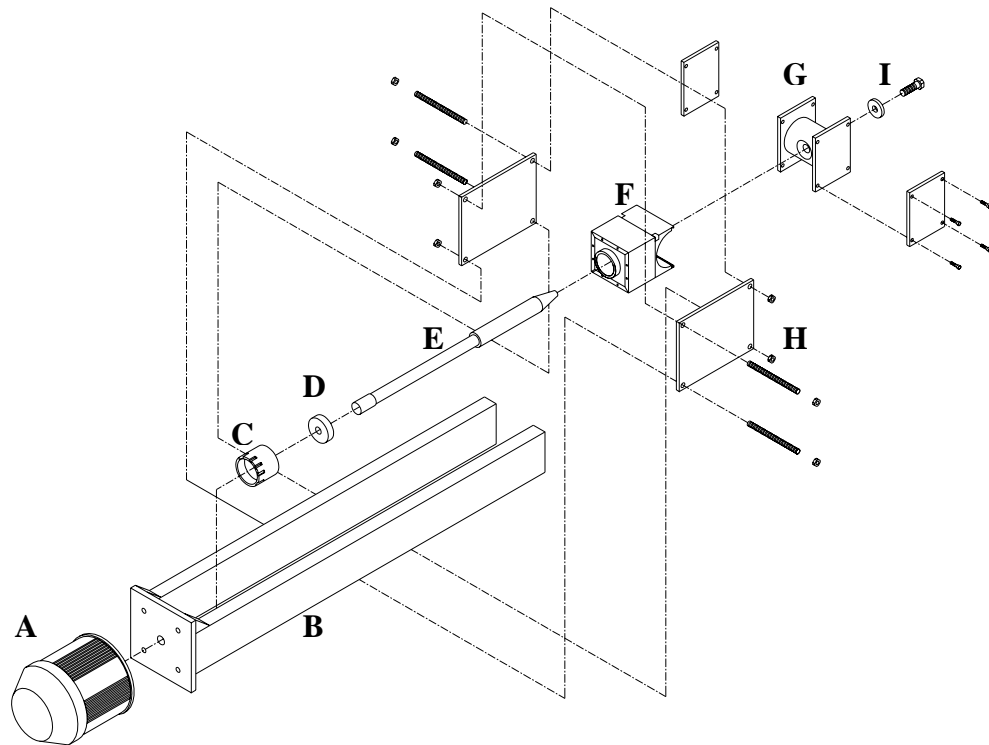
Figure 5.2. Isometric drawing of the machine setup

Legend (Figure 5.2):

A = 3 kW 1450 rpm electric motor

B = Rectangular tubular frame

C = Eccentric drive

D = Self-aligning bearing (SKF No: 2209E-2RS1K TN9/C3)

E = Test shaft

F = Environmental chamber

G = Specimen fixture with side plates

H = Cover plates

I = Fixing bolt with washer

5.2.1. Frame

Figure 5.3 shows the frame consisting of a back plate with the electric motor bolted to one side and rectangular tube legs welded to the opposite side. The whole arrangement is supported by three double U-shear rubber mountings fixed to the floor.

Eccentric drive

Rectangular tubular legs
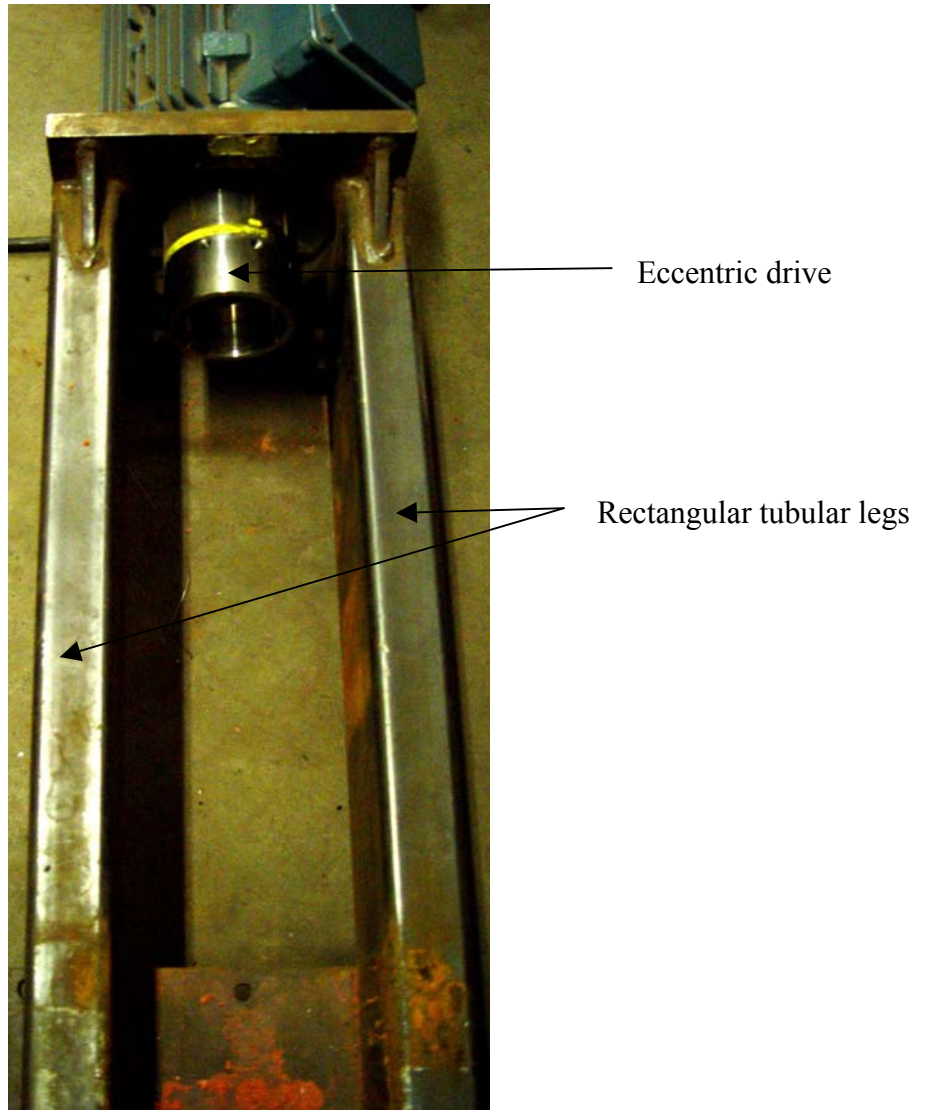
Figure 5.3. Frame and electric motor

Figure 5.4 is the drawing of the frame.

Side elevation

Rectangular tube   Cover plates

Double U-shear vibration damping mountings

Plan
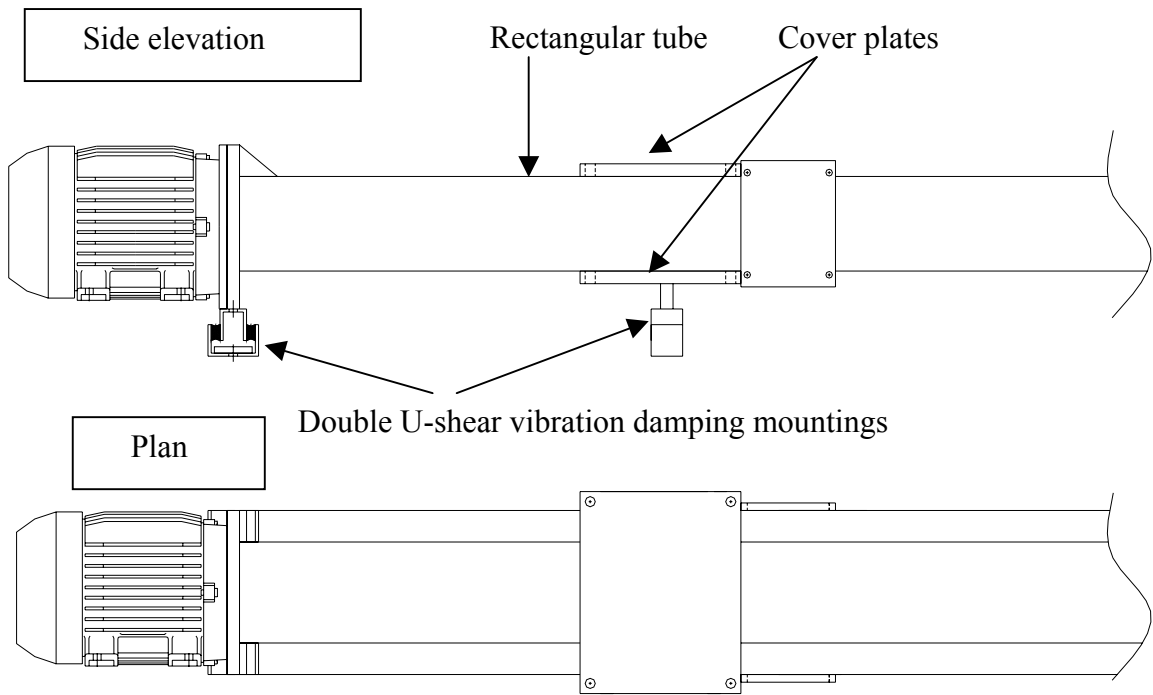
Figure 5.4. Drawing of the frame

5.2.2. Cantilever beam

Figure 5.5. Geometry of the cantilever specimen

Figure 5.6 is a drawing of the cantilever beam.

10 mm wire cut slit

775   80

40

40   35   50   20

R5   6.5°

65

510
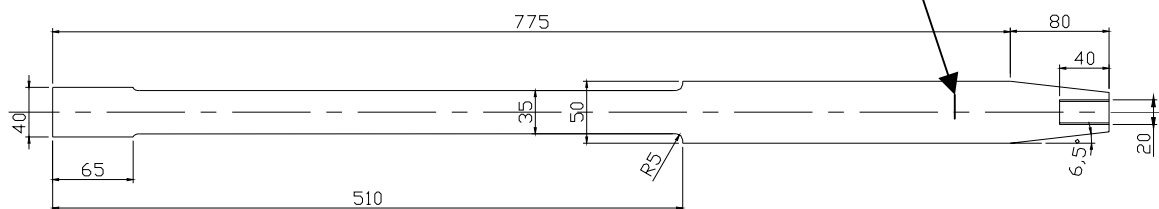
Figure 5.6. Drawing of the cantilever specimen with wire cut slit

5.2.3. Mounting block

The mounting block, for the gripping the specimen, is made from EN24 steel heat treated to the T condition. Figure 5.7 shows the mounting block with its side plates that fits between the rectangular tubular legs of the frame. The mounting block is machined with a lip to accommodate and seal one end of the environmental chamber as well as two holes allowing the measuring wires and the steam pipe to be inserted into the environmental chamber.
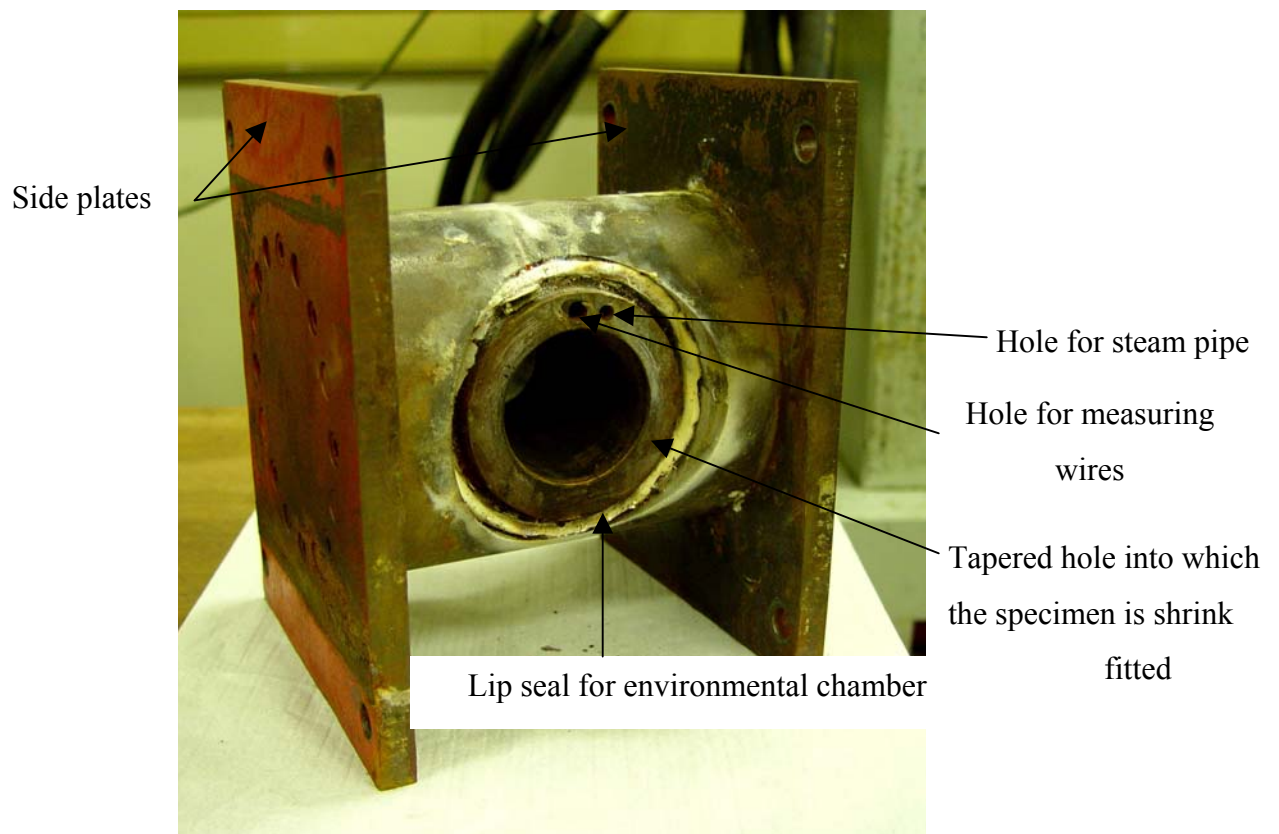
Figure 5.7. Mounting block into which the specimen fits

Figure 5.8 is the engineering drawing of the mounting block.
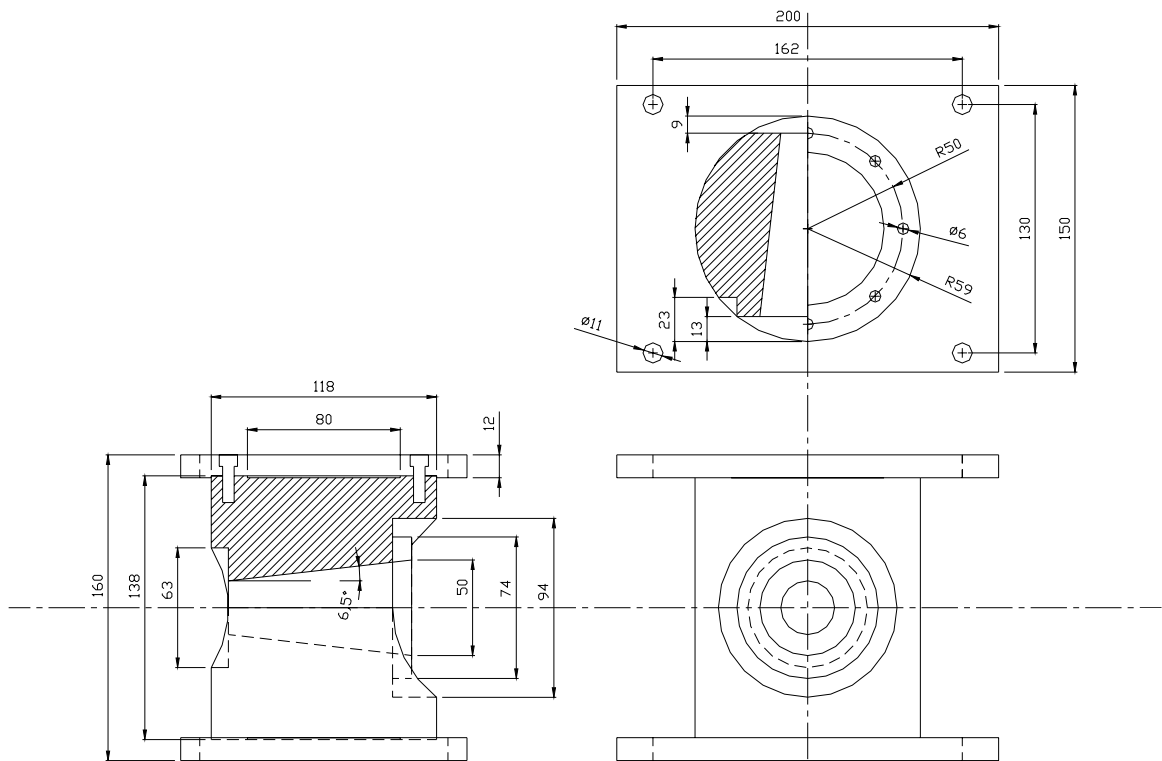
Figure 5.8. Drawing of the mounting block

5.2.4. Eccentric drive

Figure 5.9 shows the eccentric drive made from EN24 steel heat-treated to the T condition. The figure also shows the machined grooves for adjusting the eccentricity as well as the three grub screws to keep the bearing sleeve in place. The measurement tape in the figure indicates the eccentricity to which the eccentric drive is set. Reference points, of zero eccentricity, are marked on the outer surface of the eccentric drive. The deflection of the specimen is related to the relative setting of the references points on the outer surface which is indicated by the measurement tape. The specimen with the fitted self-aligning bearing fits into the sleeve as shown at the bottom of the figure while the side of the eccentric drive with the grooves (top of figure) is fixed to the shaft of the electric motor.
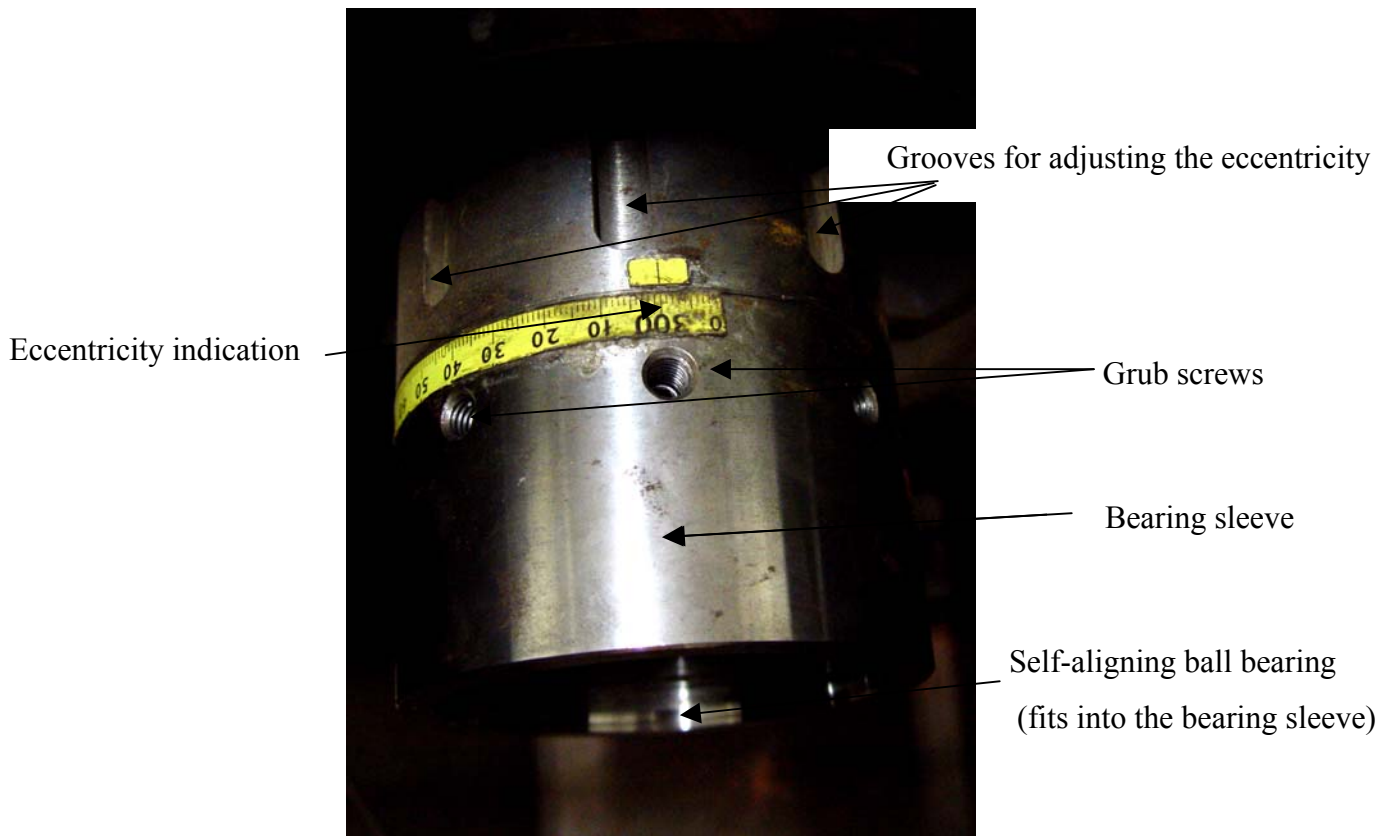
Figure 5.9. Eccentric drive to apply the load. The eccentricity is indicated by the arc length setting using the tape measure

Figure 5.10 shows details of the eccentric drive.
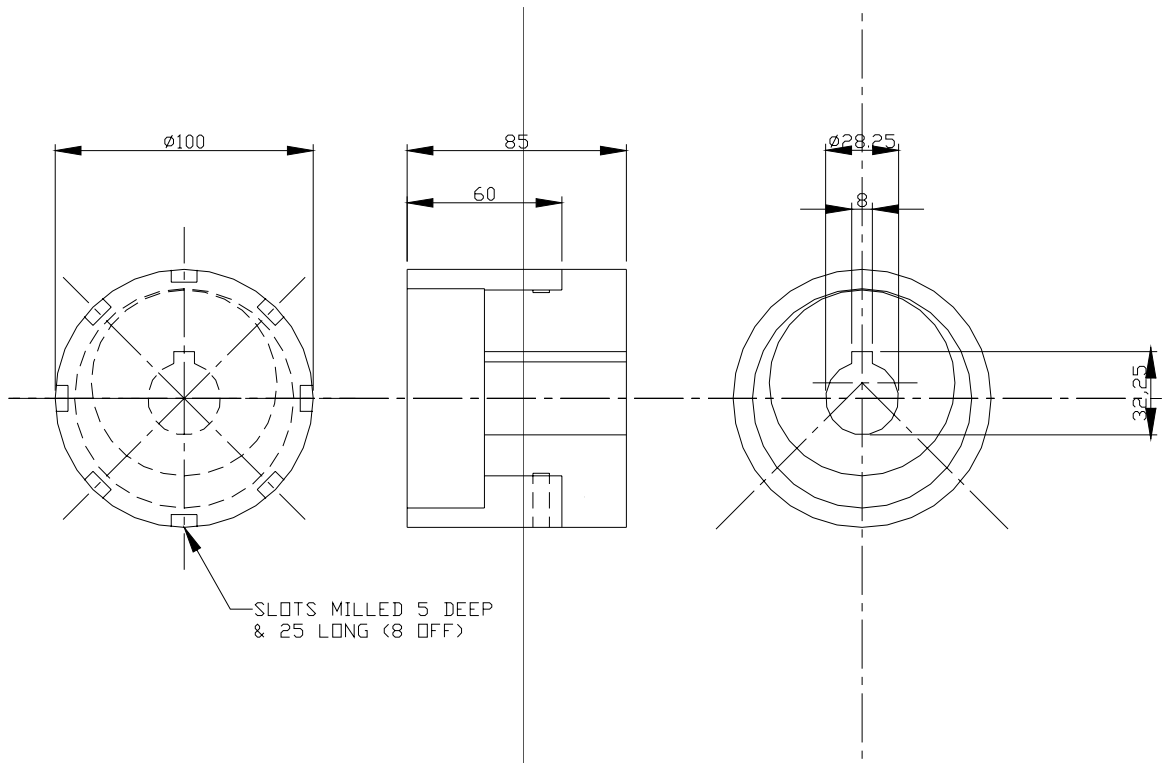
Figure 5.10. Drawing of the eccentric drive

5.2.5. Accessories

Figure 5.11 shows the accessories to adjust the eccentric drive. The 8 mm Allen key is used to undo the three grub screws, then the M8 bolt is inserted into one of the grub screw holes and is pushed against the inside of the rectangular tube leg of the frame while the C-key is used to adjust the eccentricity to the desired arc length according to eccentric indicator, at which position it is then fixed by tightening the grub screws.

Figure 5.11. Accessories to set the eccentric

5.3. ENVIRONMENTAL CHAMBER

A 1000 Watt electrically heated environmental chamber was built (shown in figure 5.12) for the high-temperature air and high-temperature steam tests.

Figure 5.12. The environmental chamber to heat the cantilever beam

Figure 5.13 shows the details of the environmental chamber.
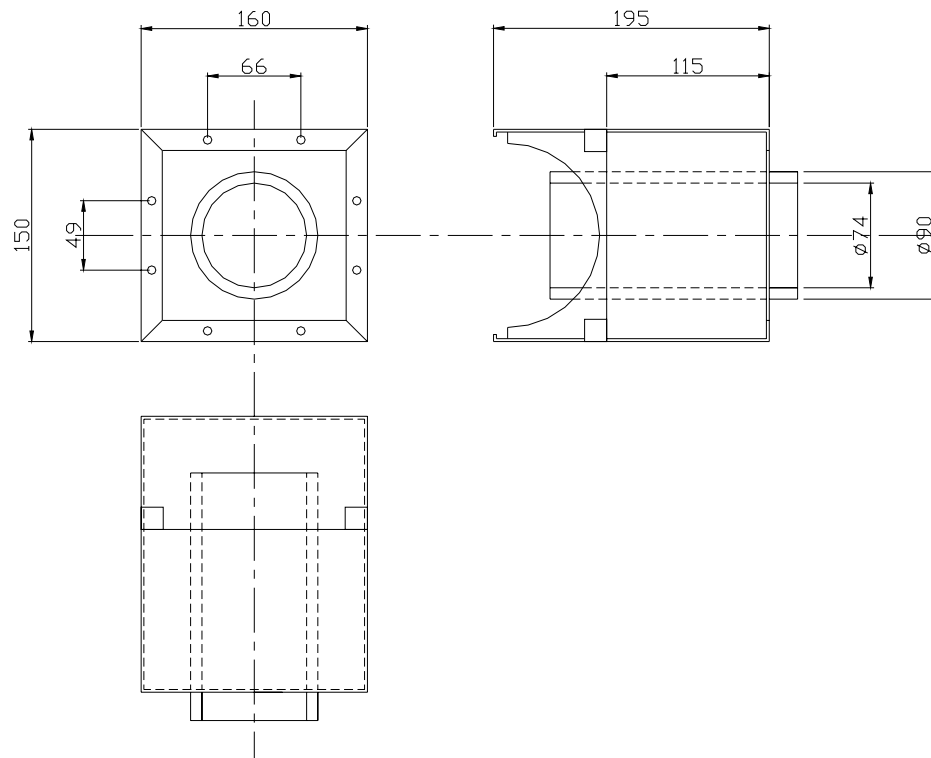
Figure 5.13. Drawing of the environmental chamber

The main chamber is manufactured from a mild steel pipe. Mica sheet is wrapped around the outer surface of the pipe to electrically insulate the Nichrome ribbon heating element wire. The element windings are kept in place by alumina cement. The space between the chamber and the stainless steel case is thermally insulated with silica wool. The environmental chamber successfully controlled the specimen temperature to within 1 ºC of the set temperature. The steam that was admitted to the environmental chamber was sealed with a specially moulded high-temperature silicon rubber cup that was clamped to the specimen and chamber by circular clamps. Sufficient positive steam pressure was maintained inside the environmental chamber to maintain an outward steam flow and to prevent atmospheric air leaking into the chamber.

5.4. STEAM GENERATION SYSTEM

Steam was generated using a hotplate and a boiler that is open to the atmosphere. Distilled water is fed into the boiler via a 20 m head pressure pipe as shown in figure

5.14. The control system for the water feed is simple and works on a mass balancing principle. The control valve is a metal plate that pushes down onto a flexible silicone tube. As water fills the boiler, the controller valve closes. As steam escapes the valve opens to let in small amounts of water to restore the balance. The energy input to the hotplate controls the amount of steam that is evaporated into the environmental chamber. The steam that is created in the boiler is above 100 °C due to the constricted outlet from the boiler. This increases the pressure above atmospheric, causing the water to boil at 117 °C. Should the system generates steam too fast, due to an excessive hotplate energy input, the pressure would increase and the inlet water be pushed back into the distilled water reservoir, causing the system to run dry. In order to maintain a positive pressure in the environmental chamber and eliminate the possibility of air entrainment, an evaporation rate of 0.3 ml water/s was found to be adequate.
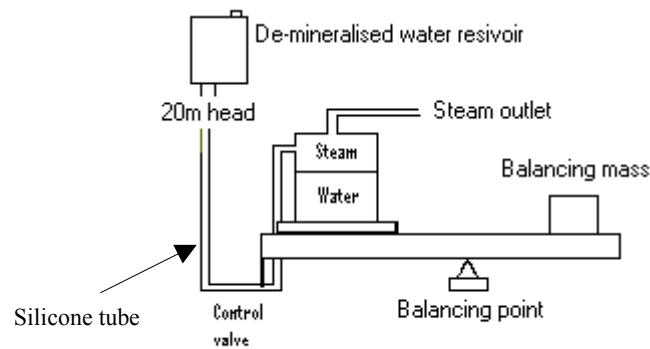
Figure 5.14. The steam generation system

6. EXPERIMENTAL WORK

6.1. MATERIAL

Low carbon steel was used during testing. The composition is shown in Table 6.1 and the microstructure in figure 6.1. A stress-relieving heat treatment at 650 °C for 5 hours was performed to relieve any residual stress in the specimen that could influence crack propagation. The average measured grain size was 30µm.

Table 6.1. Chemical composition of the steel used

Al	As	B	C	Ca	Cr	Cu	Fe	Mn
0%	0.00%	0.00%	0.12%	0.00%	0.03%	0.11%	Bal	0.57%

Mo	Nb	Ni	P	S	Si	Sn	Ti	V
0.01%	0.00%	0.09%	0.01%	0.03%	0.16%	0.01%	0.00%	0.00%
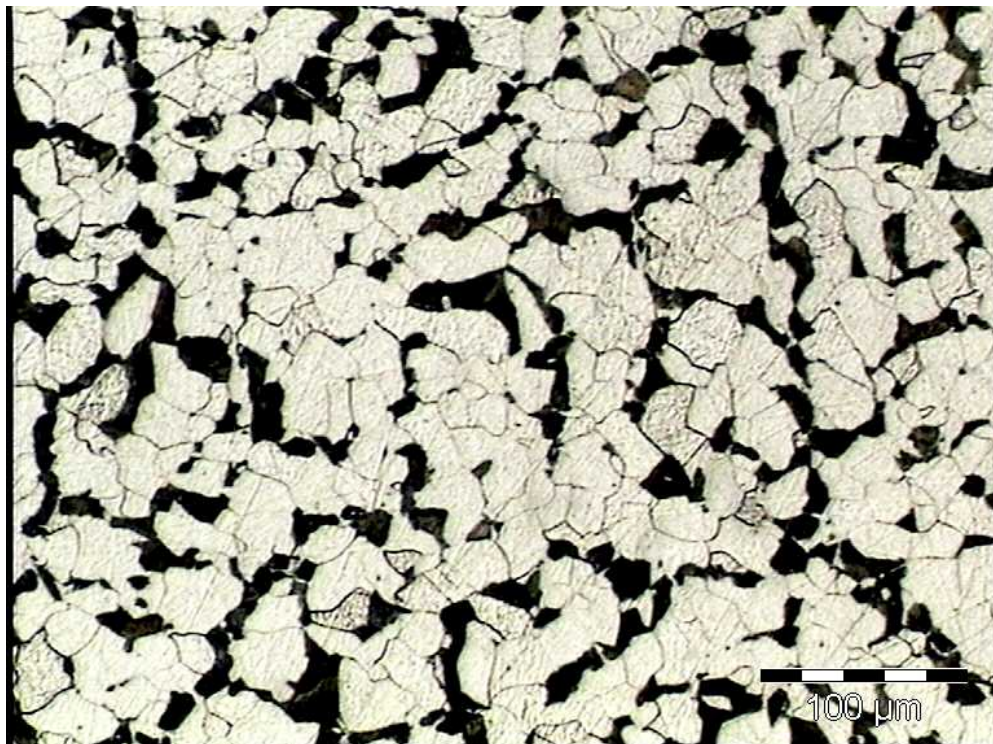
Figure 6.1. Microstructure of the low carbon steel that was used in experiments

6.2. ASSEMBLY OF THE MACHINE

The assembly sequence required for testing was as follows: first the specimen has to be fitted into the mounting block by cooling the tapered end of the cantilever beam in a mixture of ethanol and dry ice while heating the mounting block in a convection oven, thus obtaining a very tight shrink fit when they are bolted together. The crack measurement and the thermocouple wires were then spot welded into place after which the environmental chamber was positioned over the specimen, fitting into the groove on the mounting block. An airtight joint was achieved by means of a silicone sealant. The other side of the environmental chamber was sealed onto the specimen by a specially moulded silicone cup and circular metal clamps. The self-aligning bearing was then fitted to the free end of the cantilever beam. This subassembly was positioned between the legs of the frame with the bearing fitting into the eccentric drive set at zero eccentricity. The assembly was completed by securing the mounting block with side bolts and the cover plate. The holes of the measuring wires as well as the steam pipe were fully sealed with silicone rubber at the point of exit on the mounting block.

6.3. CRACK MEASUREMENT

6.3.1. Crack measurement calibration

Crack measurement was done by means of a modified Wheatstone bridge and measurements were logged on a computer using Catman software for the MGC strain gauge amplifier. Figure 6.2 shows the crack measurement setup. The AC voltage output from the strain gauge amplifier was amplified by a current amplifier to pass an AC current of 5.3 amps through the specimen. Initially the bridge was balanced by adjusting the 10-turn potentiometer. The electrical resistance of one leg of the bridge increased as the crack length increases. This caused the bridge to become unbalanced; it was rebalanced by adjusting the potentiometer. For each crack length there was a corresponding precision 10-turn potentiometer reading on the 10-turn dial indicator. The advantage of this circuit was that it compensated for resistance changes due to any variation in temperature as well as any change in the current from the current amplifier.
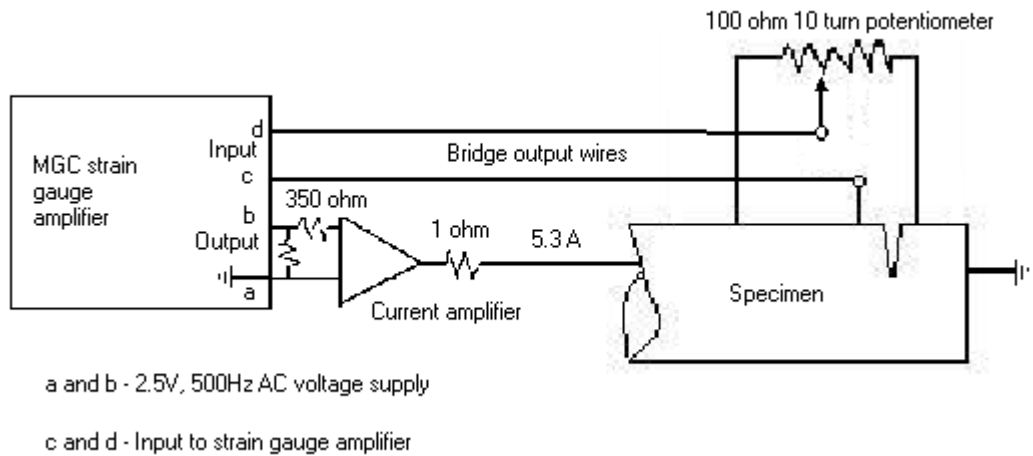
Figure 6.2. Crack measurement circuit diagram

A set of calibration samples with slits machined by wire cutting were used to generate a crack depth calibration curve. The slit depths ranged from 10 mm to 25 mm in 5 mm increments. The calibration curve is shown in figure 6.3. A linear curve was fitted to the data which was then used to determine the crack depth and finally to calculate the cyclic stress intensity range (ΔK).
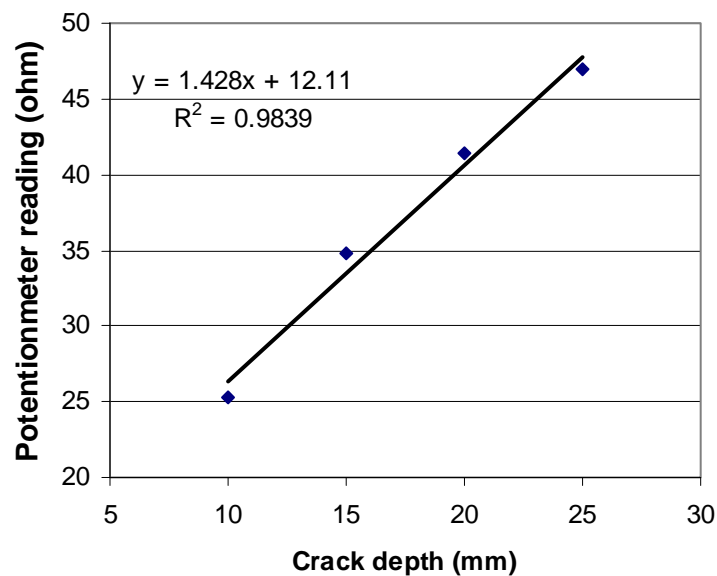
Figure 6.3. Crack depth calibration curve

Spot welding was used to secure all the wires on the specimen as well as on the crack depth calibration samples. Constantan wires 0.1 mm and 0.3 mm in diameter were used for potential and current conductors respectively to produce strong spot welds. The separate current conductors were spot welded as shown in the figure 6.4; one at 15 mm from the slit and the other at 65 mm on the opposite side of the slit. Potential conductors were spot welded as near as possible on opposite sides of the slit whilst the other bridge wire was spot welded 45 mm from the slit.
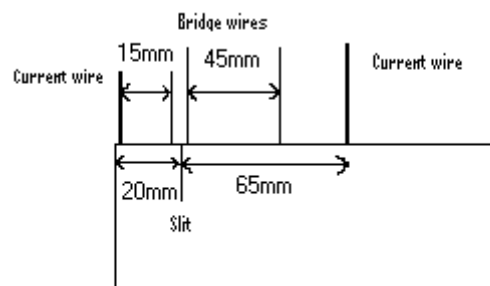
Figure 6.4. Depiction of the spot weld points

6.3.2. Crack measurement during testing

The accuracy of crack measurements was also checked by comparing the electrical measurements to optical measurements of the crack depth when the fatigue-cracked faces of the specimen were finally opened up after termination of the experiment. It was found that the difference was less then 6.2 % as long as the crack geometry stayed fairly flat without excessive curvature (see Table 6.2).

Table 6.2. Accuracy of the electrical measurement system

	Measured crack length (mm)		
Sample	Optical	Electrical	% Accurate
Air 24 ℃	15.88	15.85	99.81
Air 160 ℃	18.54	18.3	98.71
Steam 160 ℃	17.45	16.37	93.81

Figure 6.5 shows an extract of an actual record of measurements taken during testing where a mV/V reading is plotted against time in seconds. A time-proportional temperature controller was used to control the operating temperature of the environmental chamber. The magnetic field generated by the heating element current of the chamber had an interference effect on the crack measurement readings. The measurement curve became stepped; every time the temperature controller switched the chamber element on, there was a drop in the crack measurement value and when the element was turned off the crack measurement value returned to the previous measurement when no current was flowing. In order to eliminate this interference, potentiometer readings of the crack length were only taken during the off period of the heating element cycle.

It was also found, as figure 6.5 shows, that when the specimen was in the stationary position and the crack faces were not touching the crack measurements were stable. As soon as the machine was turned on, the crack measurement reading indicated a slightly shorter crack length. When the machine was turned off and the sample was placed in its original stationary position, the reading also returned to the same original baseline value. This effect is probably due to the crack faces touching during rotation, causing some shorting of the current used for measuring the change in resistance. Crack length readings were only considered when the specimen was stationary so that the crack faces were in the fully open position. A mechanical stop was used to ensure that readings were all taken in exactly the same position.

Although the magnitude of these effects was not great, they were eliminated by taking potentiometer readings only when the machine was not rotating and no heating element current was flowing. The mV/V reading during testing was only used to indicate the relative magnitude of the actual crack propagation.
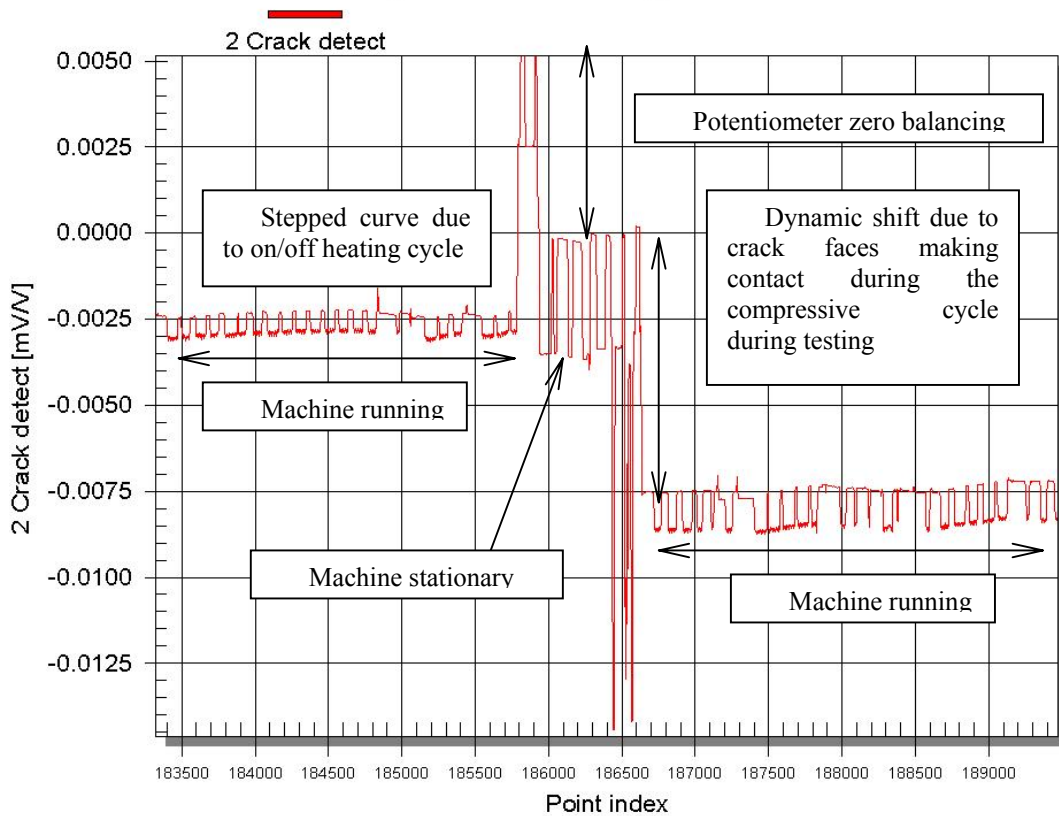
Figure 6.5. Extract of an actual record of measurements taken during testing

6.4. LOADING

The amplitude of the cyclic applied stress can be changed by adjusting the degree of eccentricity. For this purpose, part of a measuring tape was glued to the eccentric drive to indicate the arc length, as shown in figure 5.10. The actual strain at the location of the fatigue crack at any particular arc length setting was established by glueing a strain gauge to a test shaft without a slit at the position where the actual slit would be. From the amplitude of the strain value, the applied stress was calculated using a value of E = 205 GPa. This was then used as a calibration to calculate the cyclic stress intensity range during the remainder of the testing, as shown in figure 6.6. The loading cycle frequency was 24 Hz.
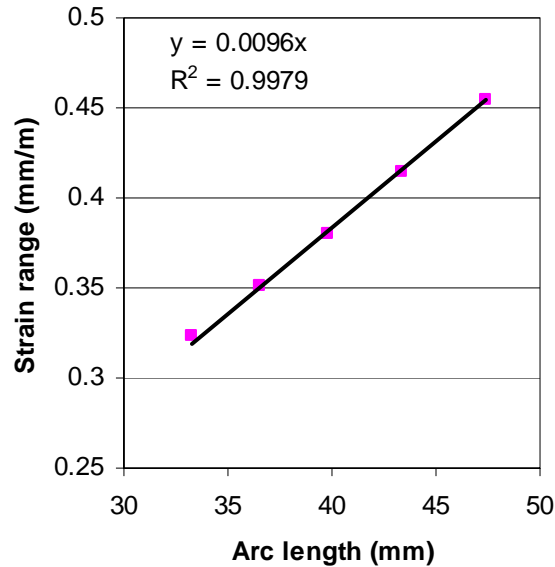
Figure 6.6. Strain calibration curve indicating the strain range in relation to the eccentric arc length

6.5. EXPERIMENTAL

In the initial tests it was found that it was not possible to fix the specimen rigidly by tightening the end bolt alone; the specimen rocked and also slowly rotated in the fixture. To stop this, the tapered end was then pressed into the tapered hole with a press. This apparently resulted in some plastic yielding at the tip of the slit and non-uniform residual stress distribution that affected the crack propagation per cycle and also the shape of the crack front. These subsequent experiments were also not satisfactory and resulted in fatigue crack fronts that were highly asymmetrical relative to the orientation of the slit (see figure 7.11 in Section 7.6). Finally, the shrink fitting procedure described previously solved the problem, thereafter the fatigue crack front propagated reasonably symmetrically relative to the position of the starter notch.

After all the experimental problems had been solved, samples were first tested in an air atmosphere at room temperature and at 160 °C, after which the threshold and the crack propagation per cycle were evaluated in a superheated steam environment at 160 °C and atmospheric pressure.

6.6. DETERMINATION OF da/dN AND ΔK

Experiments were started with a cyclic stress intensity at $\Delta K = 10\,MPa\sqrt{m}$, which was then reduced in steps of $0.5\,MPa\sqrt{m}$ to avoid premature crack closure. A crack extension of $\pm\,0.5$ mm was allowed before the next step to reduce ΔK was taken. At near-threshold values $\pm\,10^6$ fatigue cycles were accumulated in order to accurately determine the crack growth per cycle. At the threshold value 10^6 cycles were again applied to ensure that no further crack propagation occurred. If no crack extension occurred during the test period of 10^6 cycles, it was considered to be the valid measured value of the threshold cyclic stress intensity (ΔK_{th}).

The stress intensity range was calculated as follows:

$$\Delta K = K_{max} - K_{min} = YE\frac{\Delta\varepsilon}{2}\sqrt{\pi a}$$

where $K_{min} = 0$ for rotating bending

        E = Young's modulus in GPa

        $\Delta\varepsilon$ = Strain range as measured in the strain range calibration in mm/mm

        a = Crack length in m

        Y = Geometric factor

        = 1 (for $0.2 \leq \dfrac{a}{D} \leq 0.45$; see figure 6.7)
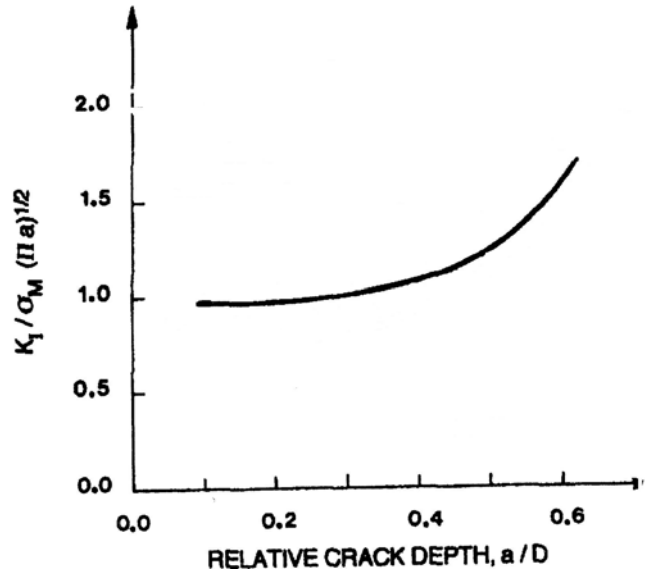
Figure 6.7. Geometric factor (Y) for straight-fronted edge cracks in a round bar under bending, where the relative crack depth is the depth of the crack in the centre relative to the diameter of the bar (Carpinteri, 1992)

Calculation of the crack growth rate per cycle:

$$\frac{da}{dN} = \frac{\left(a_j - a_i\right)}{f\left(t_j - t_i\right)}$$

where $\left(a_j - a_i\right)$ = Crack length increment in mm

$\left(t_j - t_i\right)$ = Time increment in seconds

f = Electric motor frequency = 24 Hz

7. RESULTS

7.1. CRACK GROWTH RATE VS. STRESS INTENSITY PLOTS

Using the data from tables 10.1 – 10.3 in appendix 10.1, the influences of temperature and environment on crack propagation are shown in figure 7.1. The results in figure 7.1 indicate that ΔK_{th} in air at 24 °C was $7.5 MPa\sqrt{m}$ compared with a value of only $4.8 MPa\sqrt{m}$ also in air but at 160 °C. In a superheated steam environment at 160 °C the threshold value was again $7.5 MPa\sqrt{m}$. However, at higher cyclic stress intensities, the crack propagation per cycle was about one order of magnitude lower than that in air at the same temperature. Experiments were only performed once while all the data points for the respective curves were produced from individual samples.
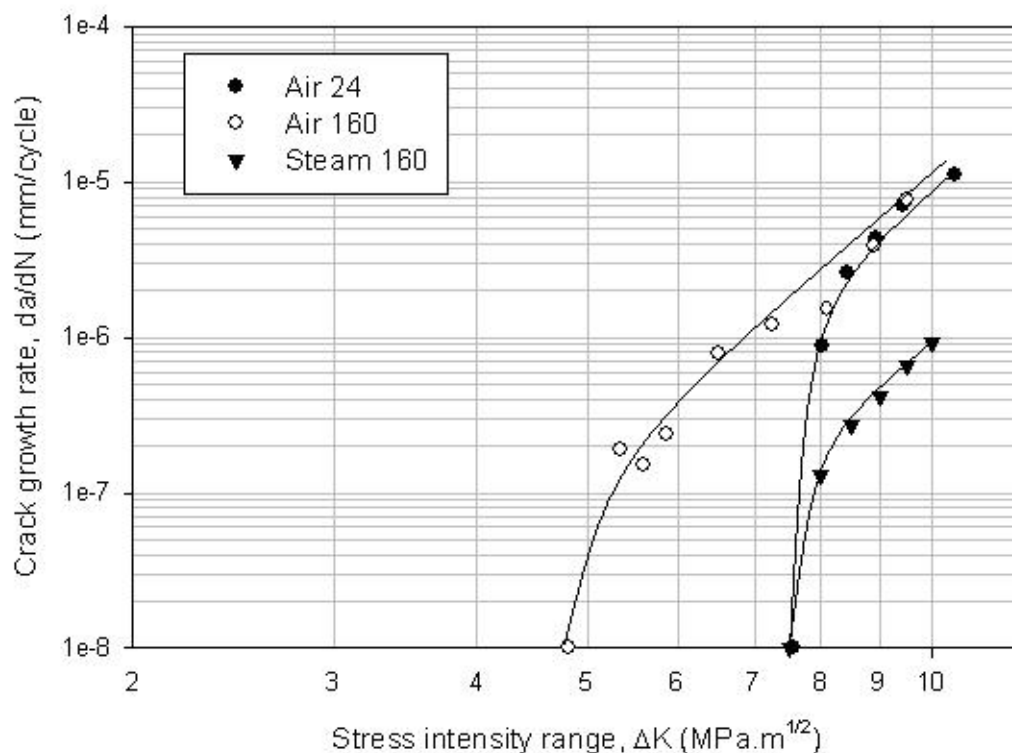
Figure 7.1. The influence of environment and temperature on ΔK_{th} in mild steel

7.2. MACROSCOPIC FRACTURE SURFACES

In figures 7.2 – 7.4 the appearance of the fracture surfaces at the location of the threshold can be seen. After the termination of an experiment the crack was opened up by way of sawing into the back ligament and forcing the crack to open with a hammer. In all these figures the starter notch can be seen starting at the top edge of the round bar, extending 10 mm into the bar and ending in a straight line. The reddish-brown colour, on the wire cut notch surface, is due to water that condensed during the shrink fitting process described in Section 2.2.

Figure 7.2 shows that in the specimen tested in air at 24 °C a distinct dark grey band of oxide formed in the vicinity of the threshold. The fracture surface was relatively clean, with at best only a thin transparent oxide layer in the region where the fatigue crack started and the crack propagation rate was high.
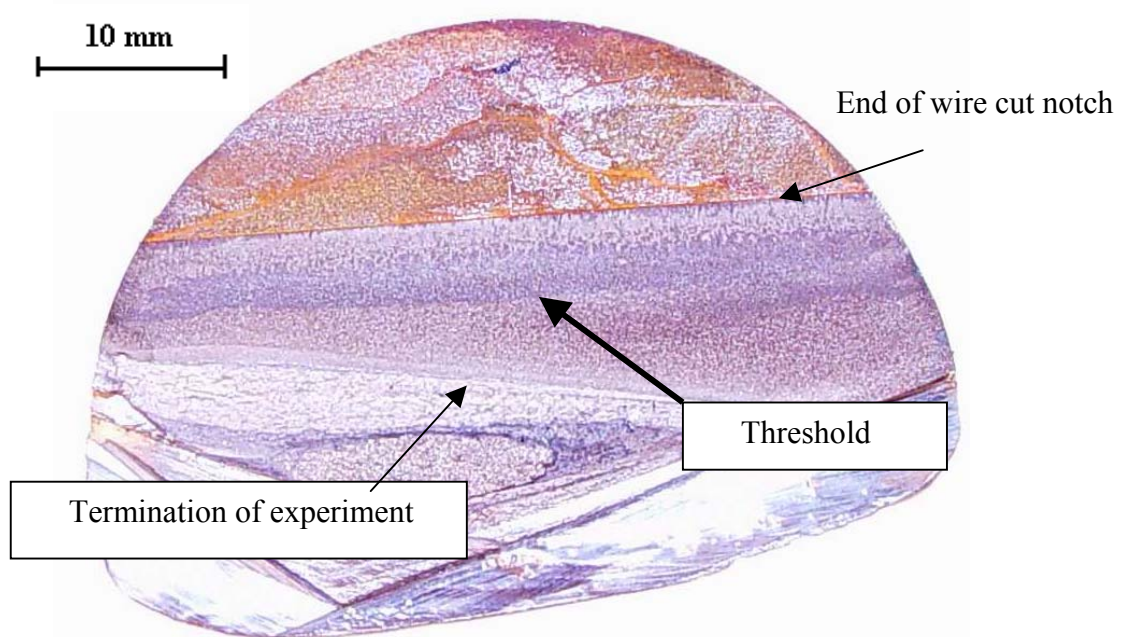
Figure 7.2. Fracture surface of the crack grown in air at 24 °C

In figure 7.3 similar features are visible for the fatigue crack propagating in air at 160 °C. In this instance the oxide that formed is scattered in patches over the fracture surface. The oxide layer appears to become thicker as the threshold front is

approached. This is indicated by the darker blue appearance of the oxide in the vicinity of the threshold.
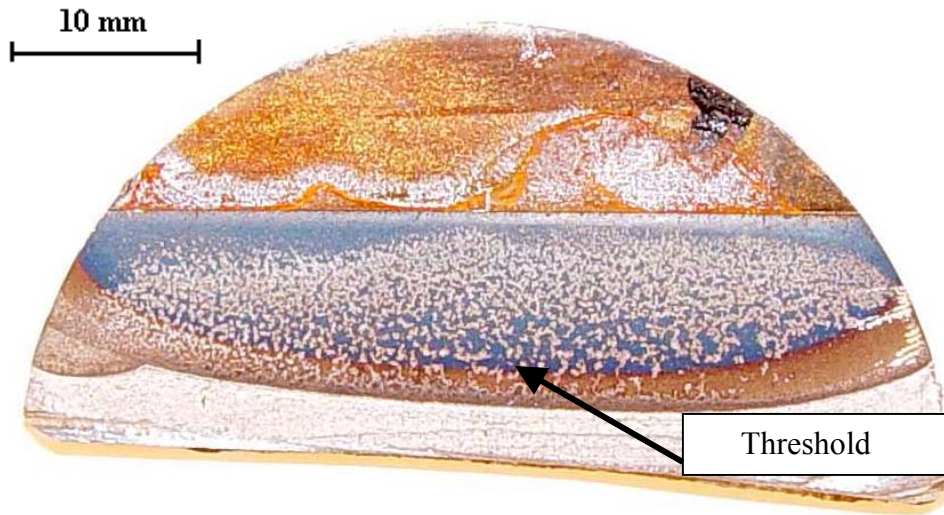
Figure 7.3. Fracture surface of the crack grown in air at 160 °C

On the other hand, figure 7.4 shows that a dark black oxide layer formed uniformly over the entire surface of the fatigue crack surface grown in steam at 160 °C.
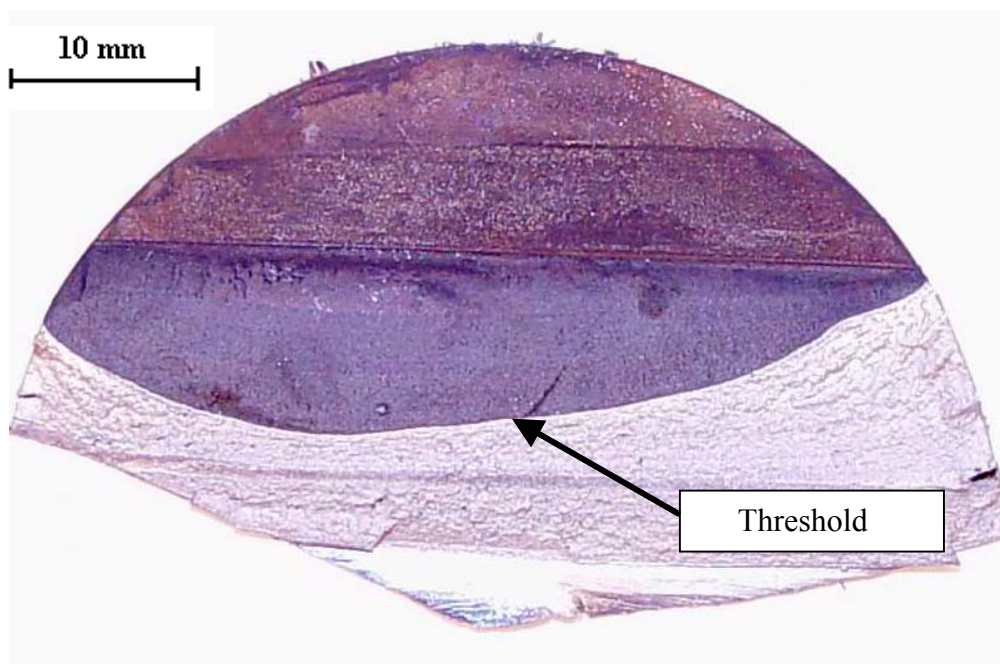
Figure 7.4. Fracture surface of the crack grown in steam at 160 °C

7.3. TRANSVERSE SECTIONS OF CRACKS

Figures 7.5 – 7.7 show transverse sections of the fracture surface in the vicinity of the threshold. The fracture surface for the specimen tested in steam at 160 °C appears less rough than that of both the fracture surfaces of the specimens tested in air at 24 °C and 160 °C. The fracture surface of the specimen tested in air at 24 °C appears to be the roughest. Yellow lines at the right hand side of these figures indicate the vicinity of the threshold.
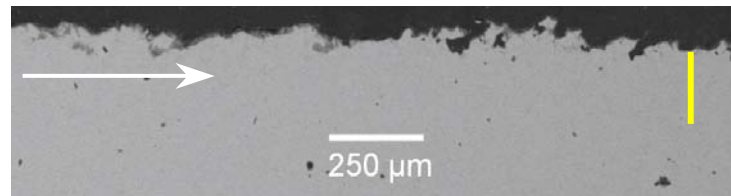
Figure 7.5. Transverse section perpendicular to growth direction in the vicinity of the threshold in air at 24 °C. Arrow indicates the direction of crack propagation
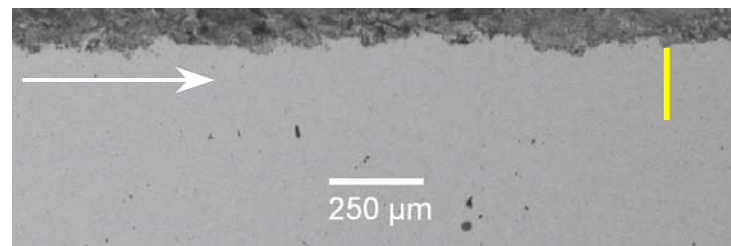
Figure 7.6. Transverse section perpendicular to growth direction in the vicinity of the threshold in air at 160 °C. Arrow indicates the direction of crack propagation
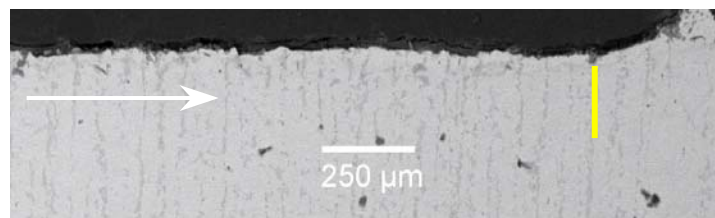
Figure 7.7. Transverse section perpendicular to growth direction in the vicinity of the threshold in steam at 160 °C. Arrow indicates the direction of crack propagation

7.4. SCANNING ELECTRON MICROSCOPE IMAGES OF FRACTURE SURFACES

Figure 7.8 shows a scanning electron microscope (SEM) image of the fracture surface tested in air at 24 °C. In the left-hand bottom corner of the image an oxide layer with a dense appearance can be seen. At the top right-hand corner of the image the exposed metal surface is visible. The fracture appearance of the metal surface appears to be mixed, with both intergranular and transgranular features. It is important to note that most of the metal surface is covered with oxide and that an exposed metal surface is the exception, with only a few spots like those shown in figure 7.8 in the vicinity of the threshold. It is probable that these patches may have originated when the oxide layer was disturbed when the crack fracture surfaces were opened up.

Figure 7.9 shows a SEM image of the fracture surface in the vicinity of the threshold of the specimen tested in air at 160 °C. Unlike the fracture surface of the test in air at 24 °C, the oxide in the top half of this image appears less dense and even flaky. In the bottom half of the image the exposed metal surface is visible. In this instance only transgranular features are visible.
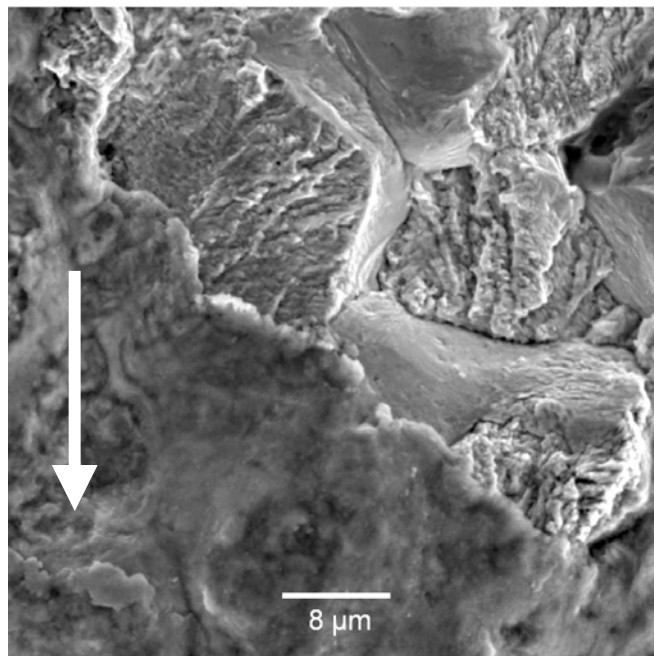
Figure 7.8. SEM image of the oxide formed (bottom left) in the vicinity of the threshold in air at 24 °C. Arrow indicates the direction of crack propagation
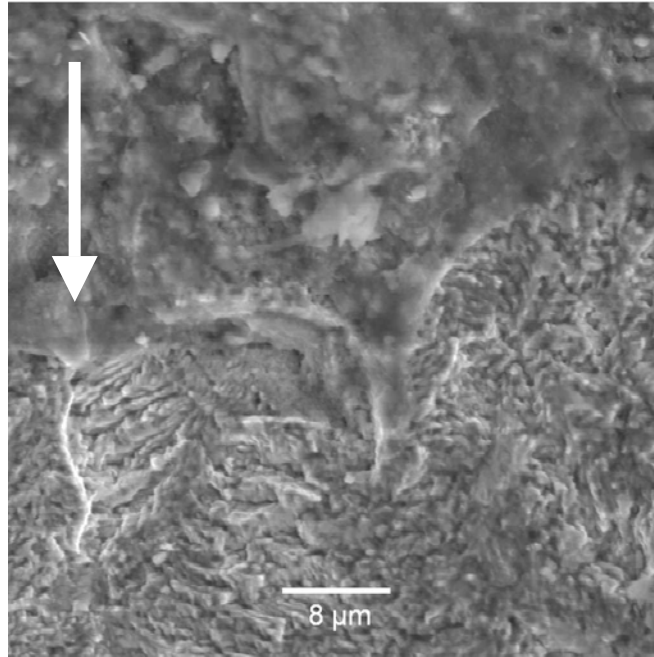
Figure 7.9. SEM image of the oxide formed in the vicinity of the threshold in air at 160 °C.
Arrow indicates the direction of crack propagation

Figure 7.10 shows an image of the fracture surface near the threshold for the specimen tested in steam at 160 °C. The whole surface was covered with a dense hard magnetite (see Section 7.5.1) layer with a crystalline morphology, with no exposed metal surfaces.
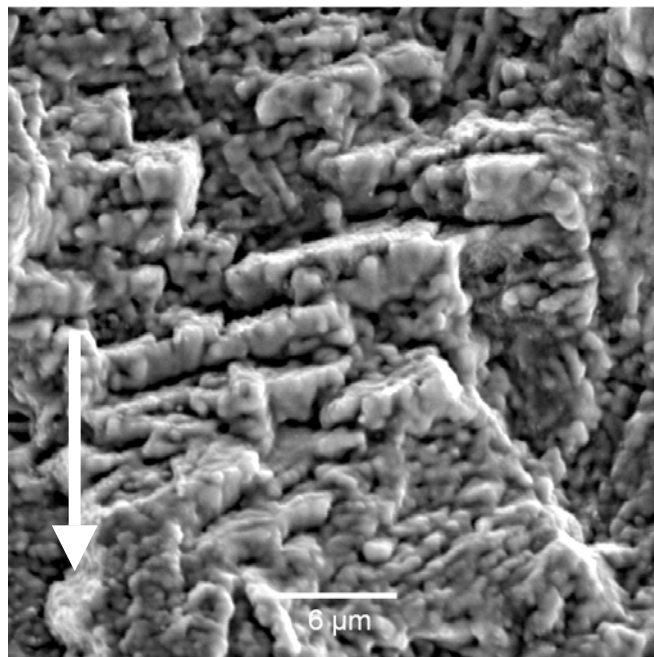
Figure 7.10. SEM image of magnetite formed in the vicinity of the threshold in steam at
160 °C. Arrow indicates the direction of crack propagation

7.5. CHARACTERISATION OF OXIDES

7.5.1. Oxide identification

Using the X-ray diffraction (XRD) results from figures 11.1 – 11.6 in appendix 11.2, the relative quantities of the different iron oxides that formed on the fracture surfaces were identified (Table 7.1):

Table 7.1. Identification of oxides that formed on fracture surfaces

Environment	Temperature (°C)	Oxide type	%
Air	24	Hematite	70
		Magnetite	30
Air	160	Hematite	74
		Magnetite	26
Steam	160	Hematite	4
		Magnetite	96

7.5.2. Oxide thicknesses at threshold

Table 7.2 shows the oxide thicknesses in the vicinity of the threshold for the current study as well as those from previous studies (Liaw, 1985 and Suresh & Ritchie, 1983). For the current study, the temper colour scale (Table 11.4) in conjunction with Auger spectroscopy was used to determine oxide thicknesses. The Auger results can be seen in appendix 10.3.2 (figures 11.7 and 11.9); a tantalum standard was used as reference.

Table 7.2. Oxide thicknesses found on fatigue fracture surfaces in the vicinity of the threshold

	Environment	Temperature (°C)	Oxide thickness (nm)		
			Auger	Temper colour	Natural
Current study	Air	24	N/A	> 70	< 8
	Air	160	62	23	< 8
	Steam	160	236	> 200	10
[2]	Air	24	9.6	N/A	0.2
	Air	149	8.7	N/A	N/A
[4]	Air	RT	200	N/A	10

N/A = Not available

7.6. OTHER RESULTS

Crack front profiles generated during preliminary testing are shown in figure 7.11. It was found that these crack front profiles were unsuitable for determining a crack length meaningfully. Crack length calibrations were performed with straight-fronted wire-cut notches because it was not practical to mechanically produce curved crack fronts. A probable reason for the peculiar curved crack fronts in figure 7.11 is probably due to the presence of uncontrolled residual stresses in the specimen, which would influence the local stress ratio at the crack front.
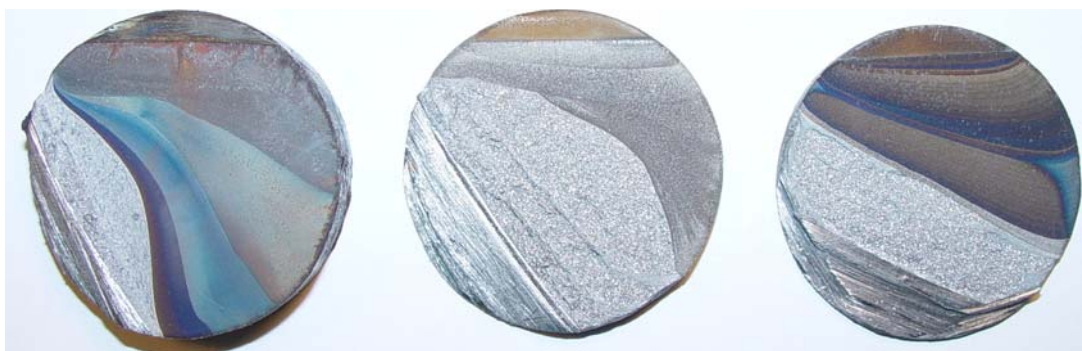

Figure 7.11. Crack front profiles generated during preliminary testing

8. DISCUSSION

8.1. MACHINE DESIGN

From the results it is clear that the custom-built fatigue testing machine simulated rotating bending successfully. The fracture surfaces that were generated are reasonably flat transverse to the direction of the maximum cyclically applied principal stress. From figures 7.2 – 7.4 it is clear that the crack front is symmetrically curved with respect to the starter notch, indicating that the crack front at the centre grew faster than the crack front near the surface. The slower growth at the edges may be due to plane stress conditions at the specimen surface as opposed to plane strain conditions at the centre of the crack front.

The fact that there is little scatter in the values of the crack growth rate curves generated is indicative of the reproducibility with which experiments were conducted. The AC potential drop crack measurement technique employed also correlated well with the optically measured crack lengths in the vicinity of the threshold.

The straight-line relationship in the Paris region for high stress intensities is given by $\dfrac{da}{dN} = A\Delta K^{m}$, where m is the slope of the fatigue crack growth rate curve. The experimental values were obtained at relatively low crack propagation rates, and from these experiments it was not possible to determine values for m.

The crack faces do not exhibit a "factory rooftop" appearance which would be expected in the presence of a large shear mode loading. This is due to the fact that was no fixed torque component was applied to the specimen and the fact that the cyclic shear stress was only 1/60 of the bending stress (see appendix 11.4).

8.2. THE EFFECT OF TEMPERATURE

In a previous study as well as the present study have shown that the threshold stress intensity value in air decreases as the temperature is increased from 24 °C to 160 °C. The decrease in the threshold value was attributed (Liaw, 1985) to a rougher fracture surface at the lower temperature, while at the higher temperature the roughness of the fracture surface was reduced, resulting in less crack closure. The oxide thicknesses on the fracture surfaces, however, were of the same order (see figure 4.6). An alternative explanation (Kobayashi, 1991) attributed the decrease in the threshold value with increasing temperature to the characteristics of the oxide, ranging from large oxide particles in the crack wake at room temperature to the formation of only a thin oxide layer at 150 °C (see figure 4.7).

The first explanation is supported by the current observations of intergranular fracture facets in the vicinity of the threshold for fatigue in air at 24 °C (figure 7.8 and figure 7.5) and an essentially transgranular fracture surface for fatigue in air at 160 °C (figure 7.9 and figure 7.6). The current experiments, however, also indicate a difference in oxide thicknesses. In air at 24 °C the oxide thickness of the dark grey band was found to be > 70 nm, whereas the thickness of the blue oxide in air at 160 °C was found to be 23 nm. These thicknesses were estimated using the temper colour scale (Beranger et al, 1996). With the Ar^+ sputtering technique employed during Auger spectroscopy, the blue oxide was found to be $\sim 60 nm$, but the thickness of the dark grey oxide of the sample tested in air at 24 °C could not be determined meaningfully using this technique. This may be due to the fact that the ion sputtering technique is sensitive to surface roughness.

During normal oxidation at 24 °C and 160 °C without fatigue, the oxide thickness was previously measured to be < 8 nm (Suresh & Ritchie, 1983). The thicker oxide layer that developed, especially in the vicinity of the threshold, is probably due to fretting oxidation. Fretting oxidation (Benoit et al, 1980) is the process whereby the oxide layer is repeatedly ruptured by relative motion between the mating fracture surfaces to expose new metal surfaces to be reoxidised. This process leads to the creation of an excessively thick oxide layer compared with that of a metal surface naturally oxidised for the same period of time in the same environment. This is illustrated schematically in figure 8.1.
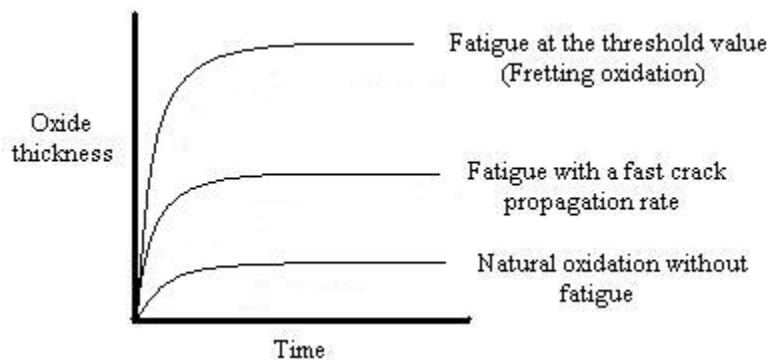
Figure 8.1. Schematic illustration of fretting oxidation compared with natural oxidation

The fracture surfaces produced at 24 °C and 160 °C had similar relative amounts of α-Fe_2O_3 and Fe_3O_4, which is indicative of the same oxidation process. In a number of studies (Smith, 1987 and Suresh & Ritchie, 1983) it was found that the threshold value is higher in the wet and moist environments than in dry environments. The increase in the threshold stress intensity value for moist environments was attributed to fretting oxidation.

From the above it is concluded that the temperature effect on the threshold value can be ascribed to roughness-induced crack closure due to the reduction in surface roughness as the temperature is increased from 24 °C to 160 °C. Oxide-induced crack closure is of main importance, since the thickening of the oxide layer in the vicinity of the threshold due to fretting oxidation seems to contribute mostly to the increase of the threshold value at 24 °C relative to that of air at 160 °C.

8.3. THE EFFECT OF THE ENVIRONMENT

In previous studies as well as the present study it was found that the threshold value increases as the environment is changed from air at 160 °C to steam at 160 °C. A study in steam and air at 260 °C (Tu & Seth, 1978) found branching cracks extending over several grains in transverse sections of the specimens tested in steam. These branching cracks were not only present in the vicinity of the threshold, but also in regions of higher stress intensities. A dark oxide layer was also found on the fracture surfaces. This oxide was not identified, neither was the oxide thickness measured. Branching fatigue cracks were also found for a stainless steel tested in an argon atmosphere (Keleştemur & Chaki, 2001). In the current study no crack branching was observed in the transverse section of the specimen tested in steam (figure 7.7).

In steam the oxide that formed on the fracture surface consisted mainly of Fe_3O_4, while a mixture of oxides formed in air. Fe_3O_4 was also found on fatigue fracture surfaces of a 508-2 steel in a light water reactor (LWR) environment at 149 °C (Cullen et al, 1983).

Inspection of figure 7.1 shows that there is an order of magnitude drop in the crack growth rate in steam at higher stress intensities compared with air at the same stress intensities. This can be explained by the fact that the black oxide (magnetite) formed uniformly over the whole fracture surface, from the starter notch to the threshold (figure 7.4). This is possibly due to the faster oxidation kinetics in a steam atmosphere during fatigue as well as the contribution of fretting oxidation. The resulting crack closure effect is therefore probably not only applicable at the threshold stress intensity level, but is also operative at higher cyclic stress intensities, resulting in lower crack propagation rates.

9. CONCLUSIONS

The following conclusions were reached:

- The custom-built fatigue testing machine to simulate rotating bending operated successfully.

- Fretting oxidation plays a major part in the thickening of oxide layers during fatigue at near-threshold crack growth rates for the environments and temperatures investigated.

- The decrease in the threshold value as temperature is increased from 24 °C to 160 °C is related to the decrease in the oxide thickness and the decrease in fracture surface roughness.

- Oxide-induced crack closure is probably responsible for the higher threshold value in steam at 160 °C as opposed to air at 160 °C. It is deduced that the oxidation kinetics in steam, during fatigue, is fast enough to also retard the fatigue crack growth rate at higher stress intensities near the threshold.

10. REFERENCES

ASTM 647-99.

Benoit D, Namdar-Irani R & Tixier R. 1980. Oxidation of fatigue fracture surfaces at low crack growth rates. *Materials Science and Engineering*, Vol. 45, pp 1-7.

Beranger G, Henry G & Sanz G (eds.). 1996. The book of steel. *Intercept*, p 579.

Bignonnet A, Namdar-Irani R & Truchon M. 1982. The influence of test frequency on fatigue crack growth in air, and crack surface oxide formation. *Scipta Metallurgica*, Vol. 16, pp 795-798.

Carlson RL & Kardomateas GA. 1994. Effects of compressive load excursions on fatigue crack growth. *Fatigue*, Vol. 16, February, pp 141-146.

Carpinteri A. 1992. Stress intensity factors for straight-fronted edge cracks in round bars. *Engineering Fracture Mechanics*. Vol. 42, No. 6, pp 1035-1040.

Cullen WH, Torronen K & Kemppainen M. 1983. Effect of temperature on fatigue crack growth of a 508-2 steel in LWR environment. *NTIS Technical Report, Springfield, VA (USA)*.

Czyryca J. 1985. Fatigue crack initiation. *Metals Handbook 9th ed*. Vol.8, pp 169-170.

Geary W & King JE. 1987. Residual stress effects during near-threshold fatigue crack growth. *International Journal of Fatigue*. Vol. 9, No. 1, pp 11-16.

Hertzberg RW. 1995. *Deformation and fracture mechanics of engineering materials*. Wiley, New York, Chapter12-13, pp 512-698.

Keleştemur MH & Chaki TK. 2001. The effect of various atmospheres on the threshold fatigue crack growth behaviour of AISI 304 stainless steel. *International Journal of Fatigue*. Vol. 23, pp 169-174.

Kemper H, Weiss B & Stricker R. 1989. An alternative presentation of the effects of the stress-ratio on the fatigue threshold. *Engineering Fracture Mechanics*, Vol. 32, No. 4, pp 591-600.

Kobayashi H, Tsuji H & Park KD. 1991. Effect of crack surface oxidation on near-threshold fatigue crack growth characteristics in A508-3 steel at elevated temperature. *Fracture and Strength '90*, Vol. 51-52, pp 355-360.

Lawson L, Chen EY & Meshii M. 1999. Near-threshold fatigue: a review. *International Journal of Fatigue*, Vol. 21, pp S15-S34.

Liaw PK. 1985. Mechanisms of near-threshold fatigue crack growth in a low alloy steel. *Acta Metallurgica*, Vol. 33, No. 8, pp 1489-1502.

Lindley TC. 1981. Near-threshold fatigue crack growth: experimental methods, mechanisms and applications. *Subcritical crack growth due to fatigue, stress corrosion and creep – Advanced seminar on fracture mechanics, Italy.* Elsevier Science Publishing, London, pp 167-213.

Lindley TC. 1997. Fretting fatigue in engineering alloys. *International Journal of Fatigue*, Vol 19, Supp No 1, pp S39-S49.

Masounave J & Bailon JP. 1976. Effect of grain size on the threshold stress intensity factor in fatigue of a ferritic steel. *Scripta Metallurgica*. Vol. 10, pp 165-170.

Schütz W. 1996. A history of fatigue. *Engineering Fracture Mechanics*, Vol. 54, No. 2, pp 263-300.

Smith P. 1987. The effect of moisture in the fatigue crack growth behaviour of a low alloy steel near threshold. *Fatigue and Fracture of Engineering Materials and Structures*, Vol. 10, No. 4, pp 291-304.

Suresh S & Ritchie RO. 1983. On the influence of environment on the load ratio dependence of fatigue thresholds in pressure vessel steel. *Engineering Fracture Mechanics*, Vol. 18, No. 4, pp 785-800.

Taylor D. 1988. Fatigue thresholds: their applicability to engineering situations. *International Journal of Fatigue*, Vol. 10, No. 2, pp 67-79.

Topper TH & Yu MT. 1985. The effect of overloads on threshold and crack closure. *International Journal of Fatigue*, Vol. 7, No. 3, pp 159-164.

Tu LKL & Seth BB. 1978. Threshold corrosion fatigue crack growth in steels. *Journal of Testing and Evaluation*, Vol. 6, No. 1, pp 66-74.

Zaiken E & Ritchie RO. 1985. On the role of compression overloads in influencing crack closure and the threshold condition for fatigue crack growth in 7150 aluminium alloy. *Engineering Fracture Mechanics*, Vol. 22, No. 1, pp 35-48.

11. APPENDIX

11.1. CRACK GROWTH RATE VS. STRESS INTENSITY DATA

Table 11.1. Data for the 24 °C air plot

ΔK ($MPa\sqrt{m}$)	10.47	9.45	8.93	8.44	8.01	7.57
$\dfrac{da}{dN}$ ($\dfrac{mm}{Cycle}$)	1.1×10^{-5}	7×10^{-6}	4.3×10^{-6}	2.6×10^{-6}	8.8×10^{-7}	$<10^{-8}$

Table 11.2. Data for the 160 °C air plot

ΔK ($MPa\sqrt{m}$)	9.5	8.9	8.1	7.25	6.51	5.87
$\dfrac{da}{dN}$ ($\dfrac{mm}{Cycle}$)	7.6×10^{-6}	3.9×10^{-6}	1.5×10^{-6}	1.2×10^{-6}	7.9×10^{-7}	2.4×10^{-7}
ΔK ($MPa\sqrt{m}$)	5.6	5.35	4.82			
$\dfrac{da}{dN}$ ($\dfrac{mm}{Cycle}$)	1.5×10^{-7}	1.9×10^{-7}	$<10^{-8}$			

Table 11.3. Data for the 160 °C steam plot

ΔK ($MPa\sqrt{m}$)	10	9.5	9	8.5	8	7.5
$\dfrac{da}{dN}$ ($\dfrac{mm}{Cycle}$)	9.2×10^{-7}	6.6×10^{-7}	4.2×10^{-7}	2.7×10^{-7}	1.3×10^{-7}	$<10^{-8}$

11.2. XRD ANALYSIS
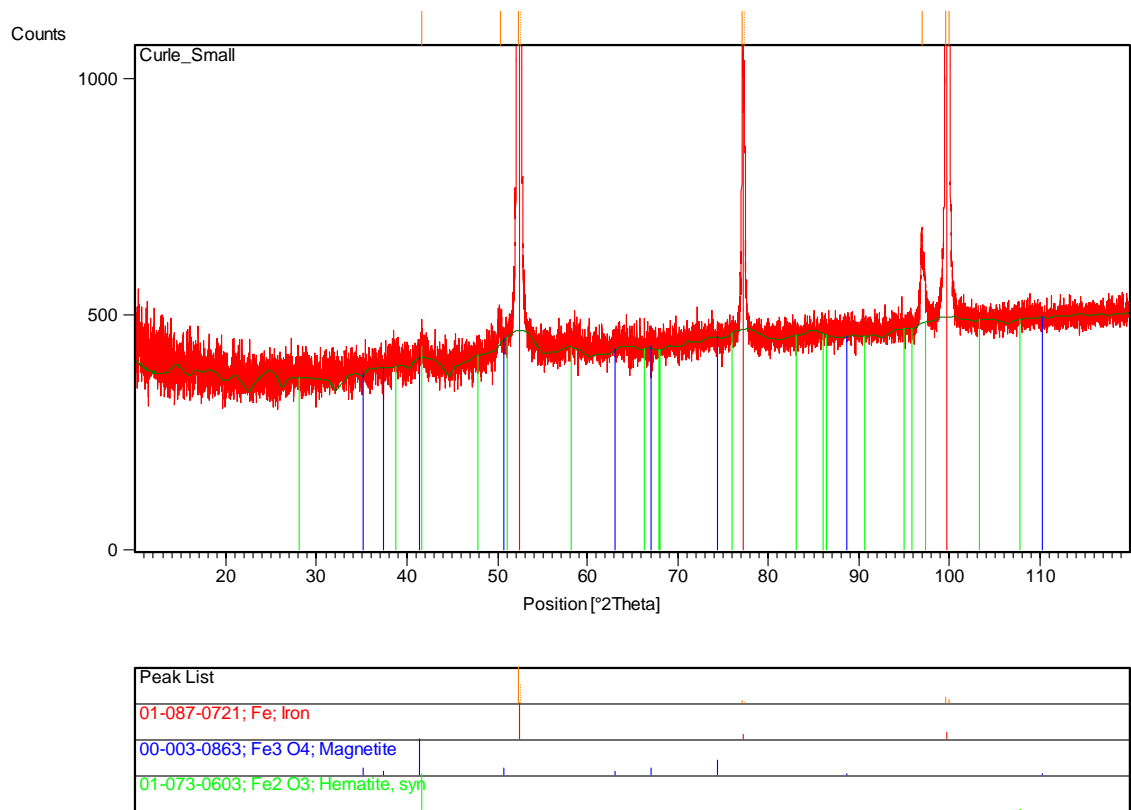
Figure 11.1. XRD pattern for the oxides on the 24 °C air fracture surface

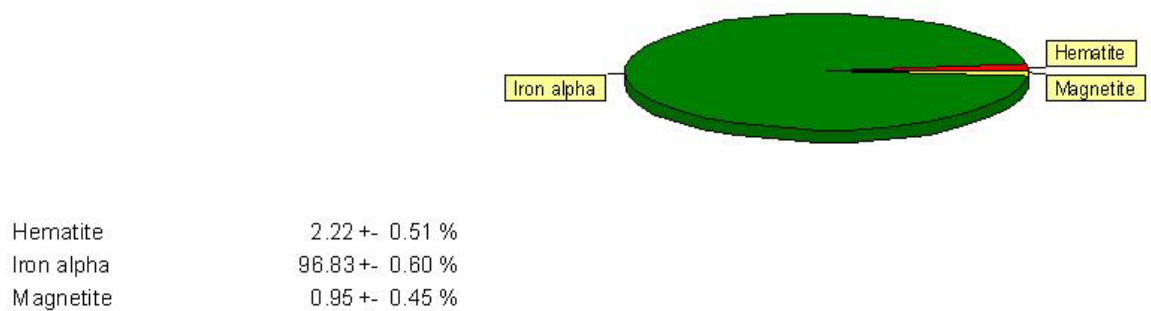| Hematite | 2.22 +- 0.51 % |
| Iron alpha | 96.83 +- 0.60 % |
| Magnetite | 0.95 +- 0.45 % |

Figure 11.2. Quantitative analysis of the oxides on the 24 °C air fracture surface
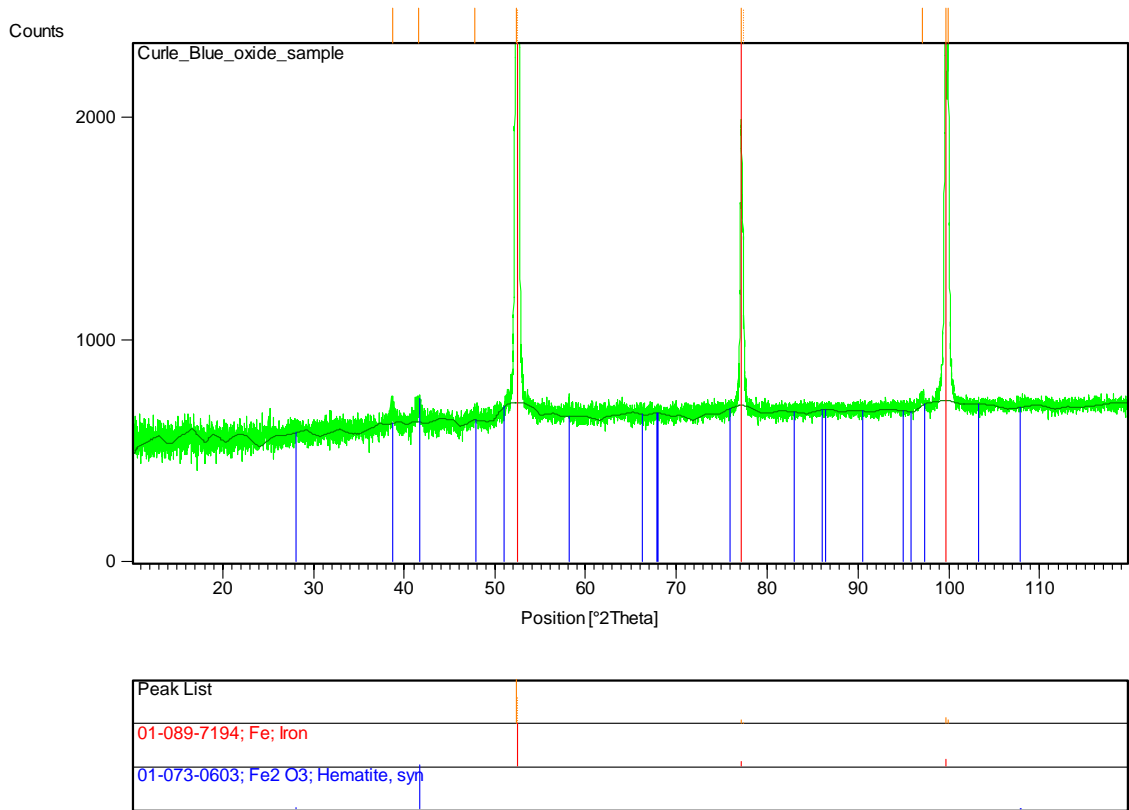
Figure 11.3. XRD pattern for the oxides on the 160 °C air fracture surface

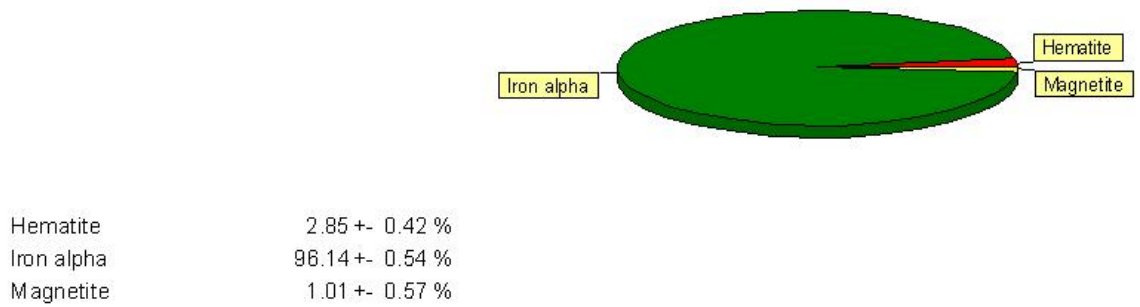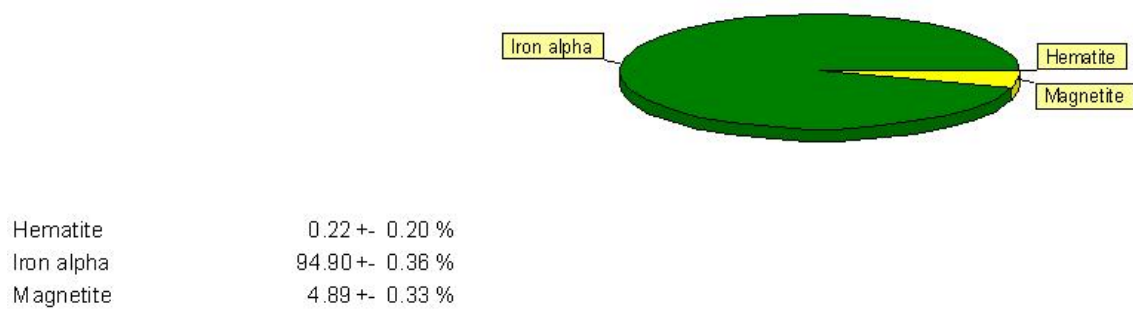|	
Hematite	2.85 +- 0.42 %
Iron alpha	96.14 +- 0.54 %
Magnetite	1.01 +- 0.57 %

Figure 11.4. Quantitative analysis of the oxides on the 160 °C air fracture surface

66
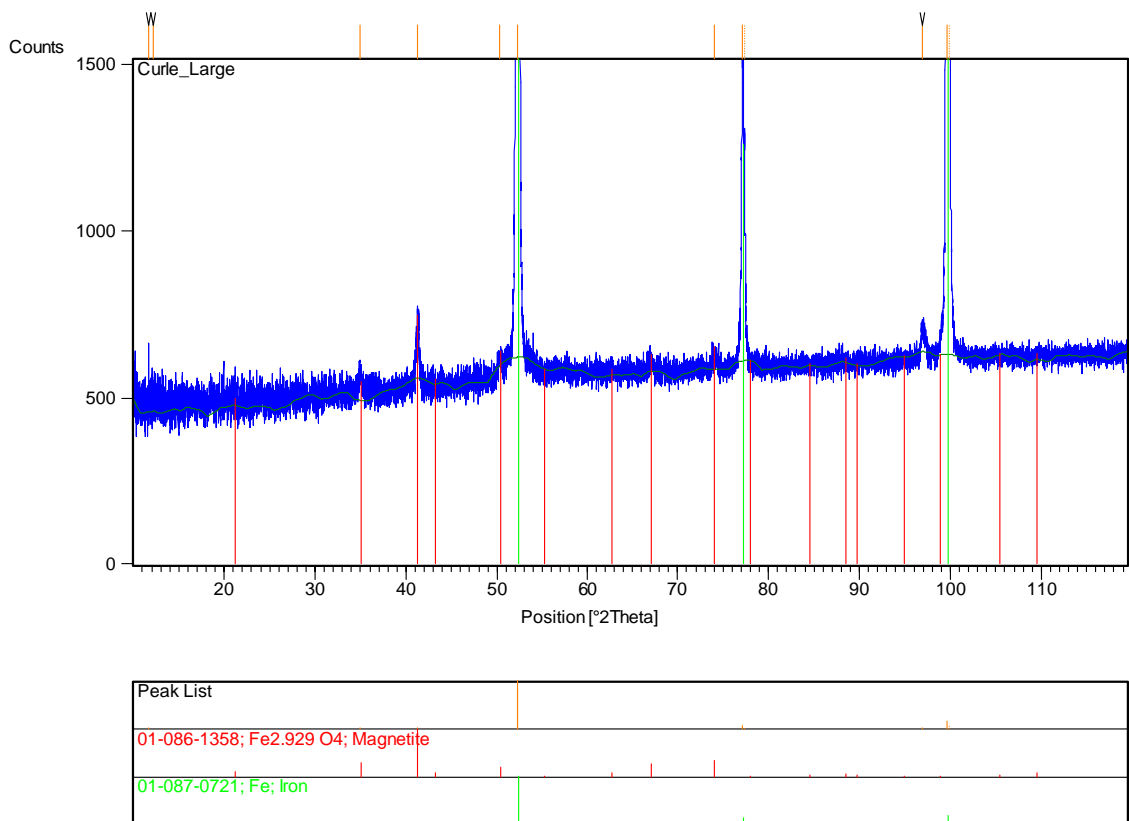
Figure 11.5. XRD pattern for the oxides on the 160 °C steam fracture surface

Hematite	0.22 +- 0.20 %
Iron alpha	94.90 +- 0.36 %
Magnetite	4.89 +- 0.33 %

Figure 11.6. Quantitative analysis of the oxides on the 160 °C steam fracture surface

11.3. AUGER SPECTROSCOPY AND SEM ANALYSIS

11.3.1. Auger setting

Survey Analyses: Beam current = 1×10^{-6} A

Beam voltage = 3 kV

Tilt angle = 30º

Depth Profile: Raster size = 1×1 mm

Ion gun voltage = 3 kV

Filament Current = 25 mA

Argon pressure = 25×10^{-3} Pa

Vacuum = 7×10^{-8}

11.3.2. Auger results
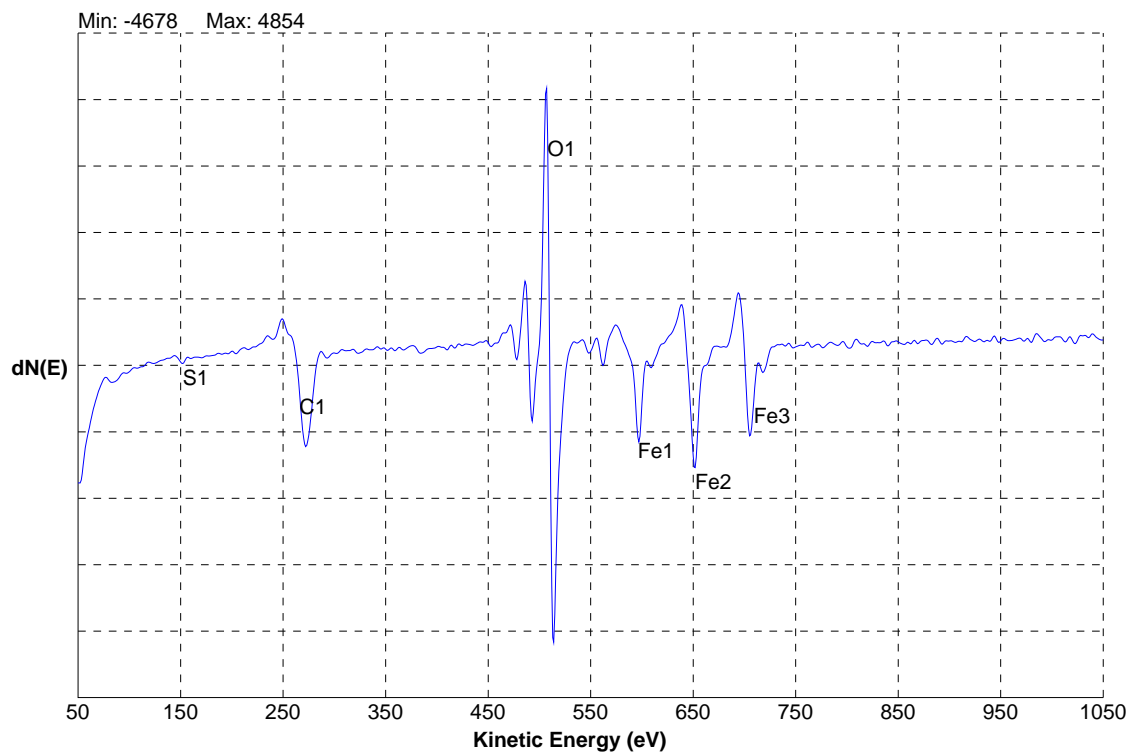
Figure 11.7. Surface spectra for the 24 °C air fracture surface
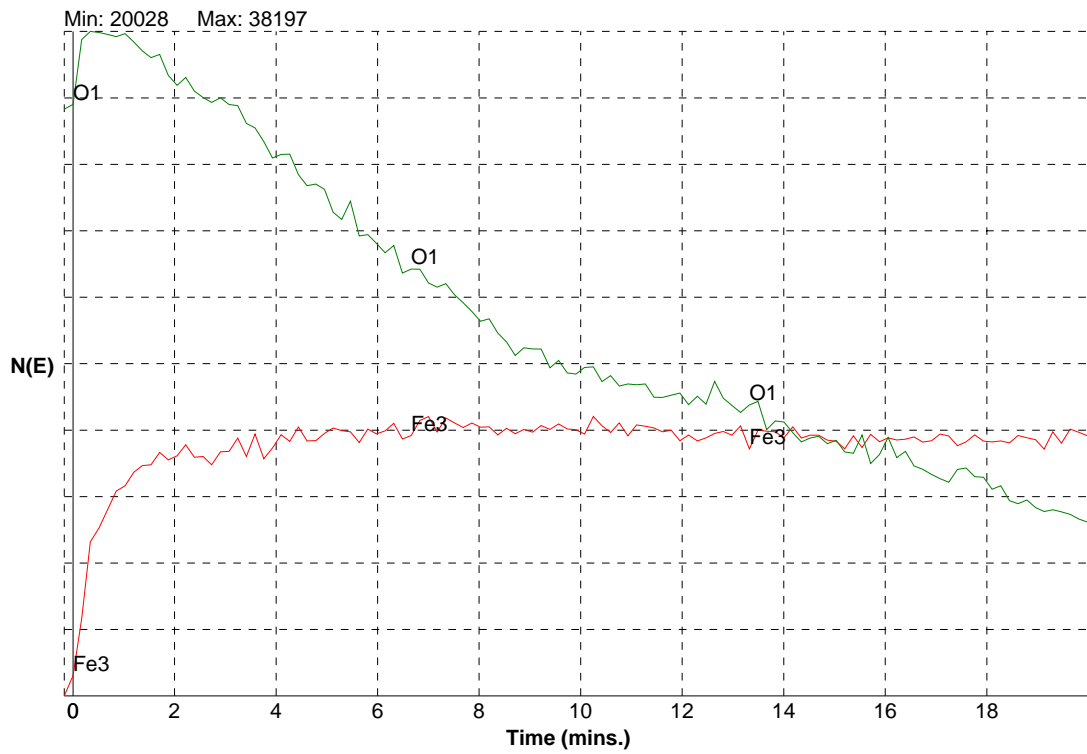
Figure 11.8. Typical depth profile of the oxide that formed near the threshold in air at 24 °C
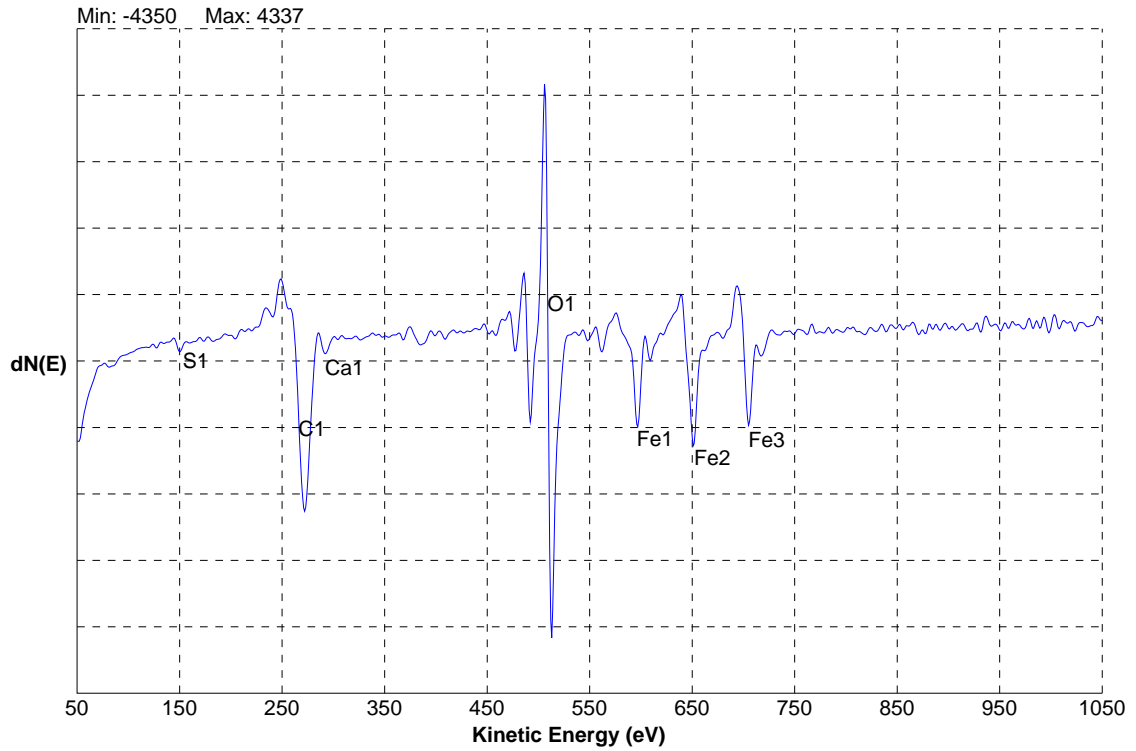

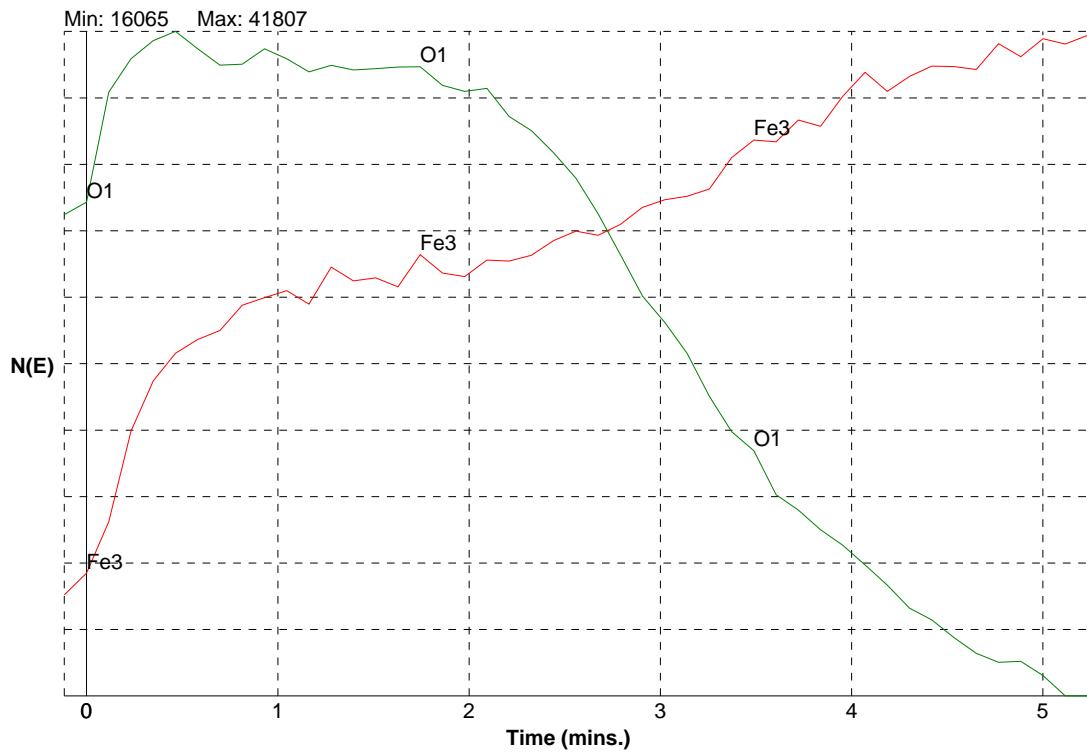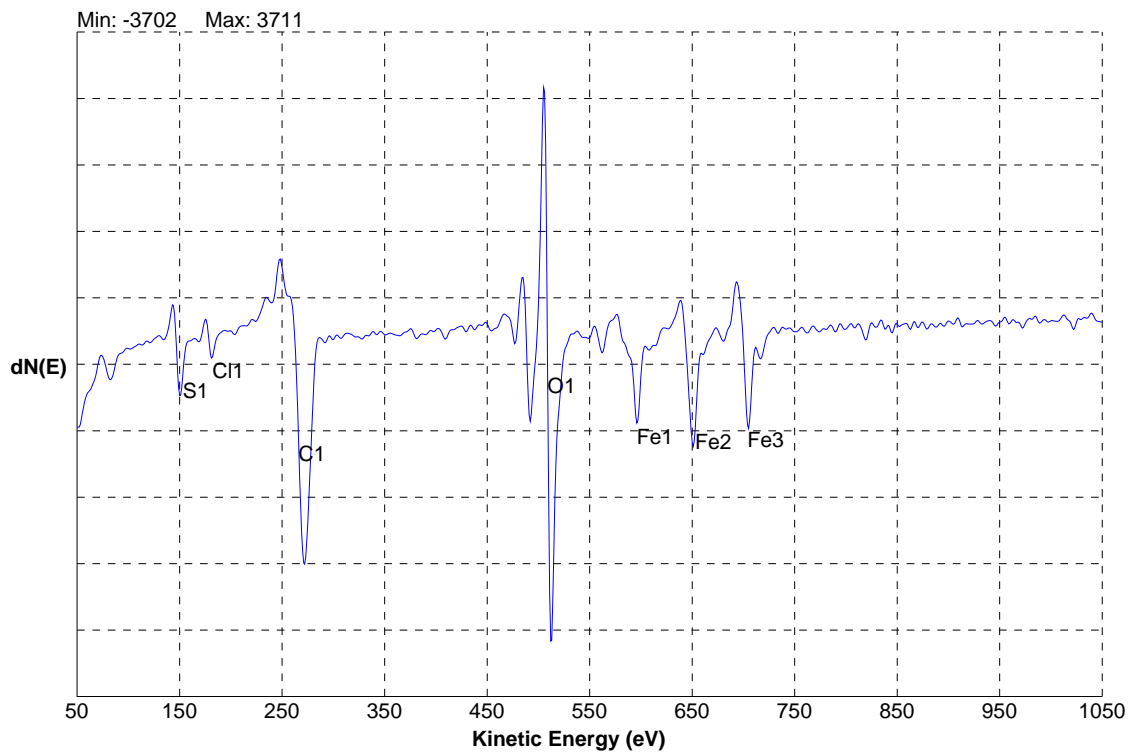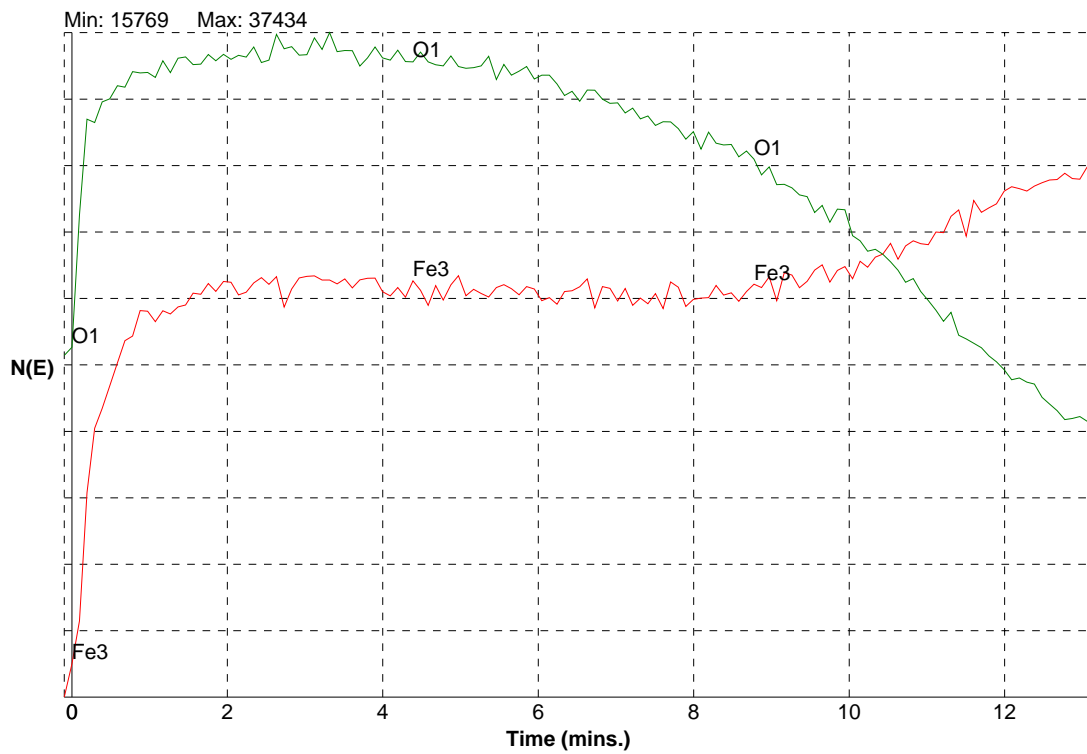**Figure 11.9. Surface spectra for the 160 °C air fracture surface**

69

Min: 16065   Max: 41807

Figure 11.10. Depth profile of the oxide that formed near the threshold in air at 160 °C

Min: -3702   Max: 3711

Figure 11.11. Surface spectra for the 160 °C steam fracture surface

Min: 15769   Max: 37434

Figure 11.12. Depth profile of the oxide that formed near the threshold in steam at 160 °C
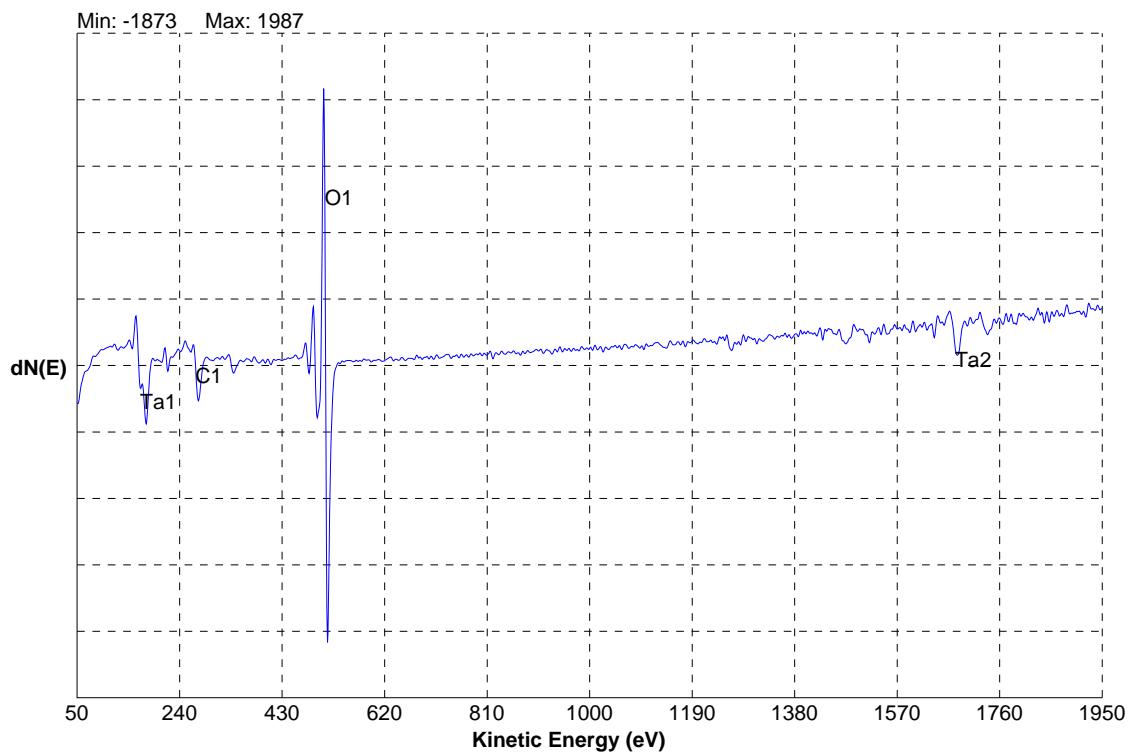
Min: -1873   Max: 1987

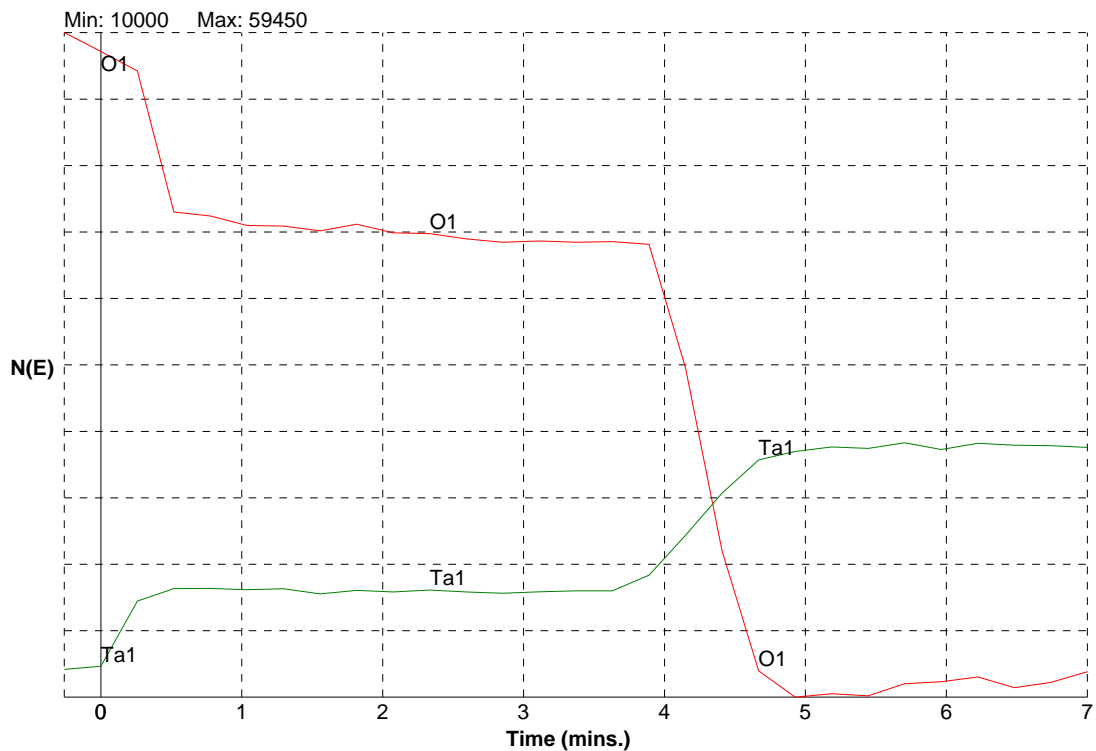**Figure 11.13. Surface spectra for a 1000 Å tantalum oxide standard**

Figure 11.14. Depth profile for a 1000 Å tantalum oxide standard

Sputtering rate for 1×1 mm raster size = 22.5 nm / min

11.3.3. The temper colour scale

Table 11.4. Temper colours as a function of oxide thickness (The book of steel, 1996)

Color	Thickness nm	Oxidation conditions	
		Temperature (°C)	Time (hours)
Straw yellow	7,7	225	0,25
Golden brown	10,3	225	2
Red-brown	13,2	225	4
Red	15,2	225	8
Deep red	15,9	250	3
Purple	18,4	250	6
Violet	21,0	250	9
Blue	22,4	250	12
Blue-green	24,4	300	2
Silvery green	30,3	300	5
Greenish yellow	35,0	300	8
Straw	38,0	300	11
Brownish gray	52,1	325	8
Pinkish gray	60,6	325	10

11.4. CALCULATION OF THE SHEAR STRESS TO BENDING STRESS RATIO
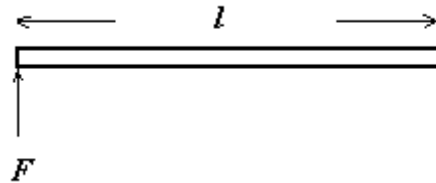
$$B.M. = F \cdot l = \sigma_b \cdot Z \qquad (1)$$

$$Z = \frac{\pi}{32} \cdot d^3 \qquad (2)$$

Substitute (2) into (1):

$$\therefore \sigma_b = \frac{32}{\pi} \cdot \frac{F.l}{d^3} \qquad (3)$$

And with

$$\tau_{max} = 2.\tau_{ave} = \frac{8}{\pi} \cdot \frac{F}{d^2} \qquad (4)$$

Divide (4) by (3):

$$\frac{\tau_{max}}{\sigma_b} = \frac{1}{4} \cdot \frac{d}{l} \qquad (5)$$

Substitution with $l = 750\,mm$ and $d = 50\,mm$ (from detailed drawing in Section 5.2.2)

$$\therefore \frac{\tau_{max}}{\sigma_b} = \frac{1}{60} \qquad (6)$$